

Hydrodynamics of insects.

Part 1. Jetting of the
dragonfly larvae.

Part 2. Honeybee at the
air-water interface: surfing
with the capillary wave

Thesis by
Chris Roh

In Partial Fulfillment of the Requirements for
the Degree of
Doctor of Philosophy

The logo for the California Institute of Technology (Caltech), featuring the word "Caltech" in a bold, orange, sans-serif font.

CALIFORNIA INSTITUTE OF TECHNOLOGY
Pasadena, California

2017
(Defended May 18, 2017)

© 2017

Chris Roh

ORCID: 0000-0002-5681-0040

ACKNOWLEDGEMENTS

First and foremost, I thank Jesus for allowing me to not lose joy even in the midst of hardship. His love (Romans 5:8) has been the constant that I held on to throughout my times at Caltech.

I thank my academic advisor, Mory Gharib, who provided guidance in my research. His inquisitiveness and audacity to tackle new problems inspired me. His creativity and wealth of experiences were solutions to many of the problems that I encounter.

I thank my thesis committee, Drs. John Dabiri, Michael Dickinson, and Gurusuwami Ravichandran, for their support and valuable comments.

I thank other lab members and friends who has been nothing but generous with their knowledge and time, teaching and discussing breadth of topics in science. I want to especially acknowledge David Kremers, who has expanded my view of art and science; Dr. Igor Siwanovic, who has provided help with the microscope imaging; Ms. Martha Salcedo who has mastered the art of finding Mory; Dr. Julia Cosse, Dr. Daegyoun Kim, Cong Wang, Nathan Martin, Dr. David Jeon, and Morgane Grivel, with whom I most frequently discussed research related qualms; all my first year buddies; and members of CCH, with whom I shared my faith journey.

To my family Dr. Taekseon Roh, Ms. Misook Lee and Seung Joon Roh, I thank them for sharing their love and wisdom and nurturing my childhood love for insects.

Finally, I thank my soon-to-be wife Jenny Han. She has provided practical help in proofreading the manuscript of this thesis and also emotional support. My final years at Caltech have been embellished with her love and care, for which I plan to repay for the rest of our lives.

This work was supported by the National Science Foundation [DGE-1144469, CBET-1511414] and the Charyk Bio-inspired Laboratory at California Institute of Technology.

ABSTRACT

This thesis presents the study on the hydrodynamics of two insects commonly known for their aerial adaptation: the dragonfly and the honeybee.

Part 1: Anisopteran dragonflies live underwater in their larval stages. The key factor for their aquatic adaptation is the modified hindgut chamber that is used as a pump. The two main functions of this biological pump are jet propulsion and respiration. Both functions involve jetting and refilling of the chamber through an orifice guard by a tri-leaflet anal valve. Despite it being a unique machinery among insects, associated hydrodynamic studies are limited thus far. In the first part of this thesis, various aspects of the hydrodynamics of the dragonfly larvae's ventilatory flow are studied. The flow visualization showed that the respiratory flow is laminar but the propulsion flow is turbulent. The hydrodynamic force analysis showed that jetting and refilling phase forces are dominated by quasi-steady momentum flux and unsteady acceleration, respectively. Finally, simultaneous measurement of the anal valve kinematics and jet flow showed that the larvae could influence the direction and magnitude of the jet by controlling the anal valve leaflets.

Part 2: Water-collecting honeybees often fall onto water surfaces. However, bees trapped by the "stickiness" of the water can propel by vibrating their wings, often making it to shore. In the second part of this thesis, the honeybee's propulsion mechanisms at the air-water interface is studied. The result shows that the bees can achieve three body-lengths per second propulsion speed. High-speed video of their wing motion shows that honeybee's propulsion involves pulling blobs of water with the underside of the wing, while pushing on a surface wave with its trailing edge. This propulsion mechanism resembles surfing on a self-generated capillary wave. Moreover, their wing vibration generates complicated surface

waves and flows, below which the deeper water flow shows a single jet stream. From the wave and flow field measurements, the average force imparted to the surrounding fluid is estimated and compared to the average force calculated from the bee's body motion. The resulting average forces are of the same order of magnitude, which means that generating wave and flow are both important for the bee's propulsion.

TABLE OF CONTENTS

Acknowledgements.....	iii
Abstract	iv
Table of Contents.....	vi
List of Figures	ix
Chapter 1 Introduction.....	1
1.1 Prologue.....	1
1.2 Organization	3
Part 1. Jetting of the dragonfly larvae	4
Part 1 Introduction	4
Chapter 2: Basic morphology and flow structure	7
2.1 Objectives	7
2.2 Materials and Methods	7
2.2.1 Confocal Microscope	7
2.2.2 Tethering Dragonfly Larvae	8
2.2.3 Flow Visualization	8
2.2.4 Flow parameters	8
2.3 Results.....	9
2.3.1 Morphology	9
2.3.2 Flow visualization	10
2.3.3 Flow parameters	12
2.4 Discussion.....	13
2.4.1 Anal valve.....	13
2.4.2 Flow Visualization and Reynolds number	13
2.4.3 Formation time	13
Chapter 3: Forces involved in reciprocal jetting of dragonfly larvae	15
3.1 Objectives	15
3.2 Materials and Methods	15
3.2.1 Animal collection and care	15
3.2.2 Experimental setup and procedure	15
3.2.3 Force measurement	17
3.2.4 Abdominal kinematics and volumetric flow rate scaling	17
3.2.5 Fluid Model	18
3.2.6 Finding C1 and C2	20
3.2.7 Area of anal orifice.....	20
3.2.8 Experiment summary table	20
3.3 Results.....	21
3.3.1 Force measurements.....	21
3.3.2 Abdominal kinematics	22

3.3.3 Case 1-4 comparisons	23
3.3.4 Impulse generated during jet propulsion	28
3.4 Discussion.....	30
3.4.1 Dominant forces during jetting and refilling phases	30
3.4.2 Impulse generated during Jet propulsion.....	31
3.4.3 Effect of tethering	31
Chapter 4: Anal valve kinematics	33
4.1 Objectives	33
4.2 Materials and Methods	33
4.2.1 Valve kinematics and quantification	33
4.2.2 Flow visualization	34
4.2.2.1 Color-coded pathline visualization.....	35
4.2.2.2 Direction of the jet	35
4.2.2.3 Particle image velocimetry (PIV).....	36
4.3 Results.....	37
4.3.1 Anal valve kinematics.....	37
4.3.2 Quantifying asymmetric opening	41
4.3.3 Degree of asymmetry and jet deflection angle.....	42
4.3.4 Deflected respiratory flow: entrainment and refilling flow	45
4.3.5 Timing of events	47
4.4 Discussion.....	50
4.4.1 Aperture size effect on respiration.....	50
4.4.2 Aperture size effect on jet propulsion.....	51
4.4.3 Effect of independent movement of the leaflet in respiration	52
4.4.4 Effect of concurrent movement of the leaflet in jet propulsion..	53
Part 1 Concluding Remarks.....	54
Part 1 References	55
Part 2. Honeybee at the air-water interface: surfing with the capillary wave..	59
Part 2 Introduction	59
Chapter 5: Honeybee at the air-water interface	60
5.1 Objectives	60
5.2 Materials and Methods	60
5.2.1 Honeybee collection and experimental setup.....	60
5.2.2 High-speed videography of an untethered honeybee	61
5.2.3 Body motion analysis.....	62
5.2.4 Tethering	63
5.2.5 Wing kinematics and wing tip velocity	63
5.3 Results.....	64
5.3.1 Wing frequency and propulsion speed	64
5.3.2 Body motion.....	65
5.3.3 Wing kinematics and interaction with water surface	66
5.3.4 Wing tip velocity.....	71
5.4 Discussion.....	71
5.4.1 Frequency and speed range.....	71

5.4.2 Wave drag.....	71
5.4.3 Model.....	72
5.4.4 Why not jump out of the water?	74
5.4.5 Comparison with other semi-aquatic insect's locomotion.....	74
Chapter 6: Flow and wave field	76
6.1 Objectives	76
6.2 Materials and Methods	76
6.2.1 Average thrust and body motion	76
6.2.2 Flow visualization	77
6.2.3 Particle Image velocimetry parameters	79
6.2.4 Shadowgraph.....	80
6.3 Results.....	81
6.3.1 Wave pattern	81
6.3.2 Flow pattern.....	82
6.3.3 Average force calculation from the body motion	85
6.3.4 Average force calculation from flow and wav field	85
6.4 Discussion.....	86
Part 2 Concluding Remarks	88
Part 2 References	89
Appendix 1	91

LIST OF FIGURES

Figure 2.1 External and internal morphology of dragonfly larvae.....	10
Figure 2.2 Flow Visualization of dragonfly larvae’s ventilatory flow.....	11
Figure 2.3 Particle pathline.....	12
Figure 3.1 Schematic of the experimental setup.....	16
Figure 3.2 Force measurements	22
Figure 3.3 Abdominal kinematics and derivatives	23
Figure 3.4 Case 1	25
Figure 3.5 Case 2	26
Figure 3.6 Case 3	27
Figure 3.7 Case 4	28
Figure 3.8 Jet propulsion impulse	29
Figure 4.1 Green algae.....	35
Figure 4.2 PIV error analysis.....	37
Figure 4.3 Area of anal opening.....	38
Figure 4.4 Full sequence of respiratory anal valve kinematics	39
Figure 4.5 Full sequence of jet propulsion anal valve kinematics	40
Figure 4.6 Asymmetry in anal valve kinematics	42
Figure 4.7 Relationship between the degree of asymmetry in anal opening and jet angle deflection	43
Figure 4.8 Directional variation of the jet.....	44
Figure 4.9 Directional variation within the respiratory jet	44
Figure 4.10 Details of the respiratory flow	45
Figure 4.11 Quantitative analysis of the entrainment flow	46
Figure 4.12 Respiratory anal valve and body kinematics and force measurement	48
Figure 4.13 Jet propulsion anal valve and body kinematics and force measurement.....	49
Figure 5.1 Schematic of experimental setup for high-speed videography.....	61
Figure 5.2 x-t diagram of the bee moving at the air-water interface.....	62
Figure 5.3 Tethered honeybee	63
Figure 5.4 Wing vibration frequency versus body speed	64
Figure 5.5 Amplitude of the honeybee’s wing vibration.....	65
Figure 5.6 Honeybee’s body position, velocity, and acceleration.....	66
Figure 5.7 Wing kinematics of freely moving honeybee	68
Figure 5.8 Wing kinematics of tethered honeybee	69
Figure 5.9 Body motion and corresponding wing motions	70
Figure 5.10 Illustration of the bee’s propulsion mechanism	73
Figure 6.1 Horizontal force balance on bee’s body.....	77
Figure 6.2 Schematics of three experimental setups	79
Figure 6.3 Wave pattern visualized using shadowgraph	82
Figure 6.4 Flow generated by a tethered bee	83
Figure 6.5 Flow velocity measurements	84

Figure 6.6 Control volume and parameter measurements.....	85
Figure A1 Jet emanating from the progressively asymmetric orifice nozzle.	91
Figure A2 Degree of asymmetry vs deflection angle	92

CHAPTER 1: Introduction

1.1 Prologue

Pervading air, water, and the interface in between, insects are found almost anywhere and everywhere on the earth's fluid environment. In adapting to these environments, they have employed diverse strategies through morphological and behavioral modifications. These adaptation strategies are great assets for science and engineering. Studying them through the fluid mechanical lens provide at least three ways science and engineering can be advanced.

First, understanding fluid mechanics of the insects gives deeper understanding of the organisms. Strange structures and behaviors displayed in insects are often understood in the context of the fluid flow that they interact with. For example, the feather-like wings of tiny flying insects would appear ineffective without knowing that fluid flows like 'honey' at the small scale.

Second, the study of their unconventional fluid interactions challenges and advances our understanding of fluid physics. Sometimes, the insects adapt to fluid environments in unimaginable ways that produce a paradox in the human mind. In resolving it, our understanding of fluid physics deepens. One of the more famous example is the flight of the bumblebees that was declared impossible using quasi-steady model. This apparent paradox was later resolved by recognizing the significant contribution that the leading edge vortex plays in lift generation. The finding highlighted the limitation of the quasi-steady model and the importance of unsteady force.

Third, the unique ways that insects interact with fluid become sources of inspiration for various engineering design problems. Broadly known as bioinspired

engineering, the relatively new field has already resulted in different inventions that were inspired by insect's interaction with fluid. One instance of this is the honeybee-mimicking 'Robobee', which is an aerial drone inspired by the flapping-wing flight of insects.

With these motivations, the author explored the hydrodynamics of dragonflies and honeybees. The use of the word hydrodynamics is by no means a mistake. Although both insects are commonly known for their aerial abilities, in certain circumstances, they also interact with water.

Dragonflies live underwater in their larval stages. During this life stage, their drastically altered hindgut functions as a water pump. A periodic compression and relaxation of the hindgut chamber results in the expulsion and refilling of water through an anal opening, which is guarded by a tri-leaflet valve. Through this reciprocal jetting, the larvae renew oxygen-deplete water for respiration, and generate thrust for propulsion.

In contrast to the dragonfly larvae's intended lives underwater, the honeybee's interaction with water is an unfortunate one. Driven by the hive's need for water, the honeybees often forage for water instead of nutritious nectar. Whether by the slight perturbation during their flight or slipping during their imbibition, the bees frequently wind up trapped on the water surface. In these circumstances, the bees were observed to propel forward, often making it to the shore.

While the aerodynamics of the dragonfly and honeybee's flight is relatively well studied, the fluid mechanical studies regarding their interaction with water are limited. To further understand the dragonfly larvae's jetting, the author studied hydrodynamic forces involved in different phases of their jetting cycle. In addition, the effect of their unique

tri-leaflet anal valve on their ventilatory flow was studied. For understanding the honeybee's locomotion at the water surface, the mechanism of thrust generation was studied.

1.2 Organization

Naturally, this thesis is divided into two parts. The studies regarding dragonfly larvae's underwater jetting is presented in Part 1, which is composed of chapters 2 to 4. Chapter 2 shows micrograph images of the dragonfly larvae's hindgut chamber and associated flow visualization. Chapter 3 identifies the main hydrodynamic forces involved during the reciprocal jetting of the dragonfly larvae. Chapter 4 discusses the functionality of the actively controlled tri-leaflet anal valve, which is unique to dragonfly larvae.

The studies regarding the honeybee's propulsion at the water surface is presented in Part 2, which is composed of chapters 5 and 6. In chapter 5, a high-speed video of the honeybee's propulsion was recorded. Their body motion and wing kinematics are observed, based on which a surfing-like propulsion model is proposed. In chapter 6, the thrusting of the honeybee at the water surface is studied through the flow and wave fields that they generate.

Part 1 and part 2 start with introductions. Each chapter is organized into statement of objective followed by methods, results and discussion. At the end of Part 1 and 2, the author provides concluding remarks, which highlight main progress made and the future directions of study.

Part 1 Jetting of the dragonfly larvae

Part 1 Introduction

Dragonflies spend up to 90% of their lives underwater as nymphs (larvae; Figure 2.1A) (Snodgrass, 1954). The key factor for the aquatic adaptation of Anisopteran dragonfly larvae is the modified hindgut chamber (Figure 2.1C), the versatility of which was noted early on by Charles Darwin—‘the alimentary canal respire, digests, and excretes, in the larva of dragon-fly’ (Darwin, 1964). The ventilatory function is divided into two modes: respiration (normal ventilation) (Hughes and Mill, 1966; Mill, 1972; Pickard and Mill, 1972, 1974, 1975; Tonner, 1936) and jet propulsion (hyperventilation) (Hughes, 1958; Hughes and Mill, 1966; Mill and Pickard, 1975).

Both respiratory and propulsion ventilation modes of the dragonfly larvae involve a periodic compression and relaxation of the hindgut chamber. This results in the expulsion and refilling of water through an anal valve opening, which is called reciprocal jetting. Through contraction of several abdominal muscles, the larvae compresses its chamber (Pickard and Mill, 1972; Mill and Pickard, 1975). Through restoration of the bent elastic exoskeleton and contraction of the diaphragm and sub-intestinal muscles, the larvae refills its chamber (Pickard and Mill, 1972; Mill and Pickard, 1975).

During respiration, the larvae remain immobile by attaching to an object and use periodic jetting for respiratory gas exchange at the surface of the chamber (Hughes and Mill, 1966; Kohnert et al., 2004). During jet propulsion, the larvae expel powerful jets for swimming, followed by a refilling phase. The late instar larvae can attain swimming speeds of up to $50 \text{ cm}\cdot\text{s}^{-1}$ (10 BL/s; Hughes, 1958). Among insects, the use of jet propulsion (Mill

and Pickard, 1975) and reciprocating water flow for respiration (Mill, 1972; Pickard and Mill, 1974), i.e. aquatic tidal breathing, is only found in dragonfly larvae.

One of the main fluid mechanical challenges in understanding reciprocal jetting is the hydrodynamic forces during the jetting and refilling phases. Various models have been utilized to understand these forces during the swimming of the jellyfish, a more frequently studied reciprocal jetter. Daniel (1983) used quasi steady model, Thrust $\sim \rho Q^2 / A$, for both jetting and refilling, where Q is the volumetric flow and A is the jet exit area for jellyfish. However, because the nature of the jetting cycle is periodic, a traditional quasi-steady thrust analysis is insufficient. The unsteady effect has been taken into account in many studies. The effect of unsteady rollup of the vortex ring in over-pressurization of the chamber has been studied (Dabiri, 2009; Krueger and Gharib, 2003, 2005). More recent study by Krieg and Mohseni (2015) showed that while the quasi-steady term dominates the jetting phase, an unsteady term dominates the refilling phase.

Another aspect of the reciprocal jetting that needs further investigation is how the flow is modulated. For dragonfly larvae, their most distal valve, known as the anal valve, is expected to play a critical role. The anal valve consists of three leaflets with individually connected retractor muscles originating from the sidewalls (Figure 2.1B, D; Mill and Pickard, 1972, 1975; Rich, 1918; Scott, 1905; Tonner, 1936). Previous studies have shown that the anal valve movement is controlled and synchronized with the jetting and refilling of the chamber in the larvae. For both propulsion and respiration modes, the jet exit is small during the jetting phase and large during the refilling phase.

Several studies have suggested the importance of anal valve movement in the appropriate functioning of jet propulsion and breathing (Hughes, 1958; Mill and Pickard, 1972; Tonner, 1936). Hughes (1958) suggested that the valve constriction enhances the propulsive thrust, and valve widening allows for efficient suction. Mill and Pickard (1972) discussed how the constricting and widening of the orifice during the jetting and refilling phases could help prevent reinhalation of the previously jetted fluid.

CHAPTER 2: Basic morphology and flow structure

2.1 Objectives

This chapter introduces the dragonfly larvae's hindgut morphology and their ventilatory flow structure. The chamber morphology is imaged using confocal micrography. A laser induced fluorescence (LIF) visualization of the dragonfly larvae's ventilatory jet is reported for the first time. Some qualitative comparison is made between the respiratory jet and propulsion jet. In addition, two important non-dimensional parameters, Reynolds number (Re) and formation time (\hat{T}), are reported.

2.2 Materials and Methods

2.2.1 Confocal Microscope

Dragonfly larvae ~1 cm in length were used for microscopy. Their hindgut apparatus was dissected out and fixed in 2% formaldehyde in phosphate-buffered saline (PBS) for 4 h. The specimens were washed with PBS containing 0.01% TritonX-100 (PBS-T) for 30 min and placed in PBS containing 6% agarose. The specimens were cut into 300- μ m slices by using a Leica VT1000S vibratome (Leica Biosystems Inc., Buffalo Grove, IL, USA) and placed in a 2-ml eppendorf tube containing 1 ml PBS-T. A couple of drops of rhodamine-conjugated phalloidin (Life Technologies, Carlsbad, CA, USA) and calcofluor white (fluorescent brightener 28; Sigma, F3543-1G, St. Louis, MO, USA) were added for overnight staining of muscle and chitin, respectively. After staining, specimens were washed with PBS-T three times for 20 min and once for 60 min. The stained slices were imaged using a Zeiss LSM710 confocal microscope (Zeiss, Oberkochen, Germany).

2.2.2 Tethering Dragonfly Larvae

Dragonfly larvae ~3-4 cm in length was tethered onto a metal rod using dental wax. The procedure is as follows. The dragonfly larvae's thorax was dried using tissue paper. The metal rod with a loop at one end was prepared. The diameter of the loop is approximately the width of the dragonfly larvae. A drop of dental wax was melted onto the loop. Any heating tool can be used; the melting point of the dental wax is approximately 50°C. The metal rod with wax was gently pushed onto the larvae's dried dorsal thorax. After about 10 seconds, the dental wax solidified. Depending on how well the larvae was connected, a small amount of dental wax was added using a tweezer to reinforce the tether.

2.2.3 Flow visualization.

The tethered larvae was placed in a glass water tank. Diluted rhodamine 6G (Sigma-Aldrich) or milk was injected into the fluid near the larvae's anal opening. The dye or milk was sucked in during the refilling phase, and expelled out during the jetting phase. The flow was illuminated using a 532 nm continuous laser sheet (Wicked Laser 1W), and the visualized flow was captured by high-speed camera (Dantec NanoSense Mk-III; Skovlunde, Denmark) at 300 frames per second.

2.2.4 Flow parameters

Flow speed, anal valve opening, and duration of the jetting are measured to approximate the Reynolds number and formation time. The anal valve size was filmed using high-speed camera. The flow speed is measured by the length of the particle streak. Details of the measurement setup and the particle used is described in sections 3.2.2 and 4.2.2.

Reynolds number (Re) is defined as

$$Re = \frac{UD}{\nu} \quad (2.1),$$

and formation time (\hat{T}) is defined as

$$\hat{T} = \frac{UT}{D} \quad (2.2),$$

where U is the jet flow speed, D is the diameter of the anal valve opening, T is the duration of jetting, and ν is the kinematic viscosity of the water.

2.3 Results

2.3.1 Morphology

The micrograph images of dragonfly larvae's hindgut chambers are shown in figures 2.1C and D. The dragonfly larvae's hindgut chamber is surrounded by radial muscles. The chamber is divided into two sections: the branchial chamber and vestibule. These compartments are divided by a series of three valves. The pre-branchial and post-branchial valves are sphincter valves, controlled by the radial muscles. The anal valve is a tri-leaflet valve with retractor muscles connected to each leaflet (Figure 2.1B, D).

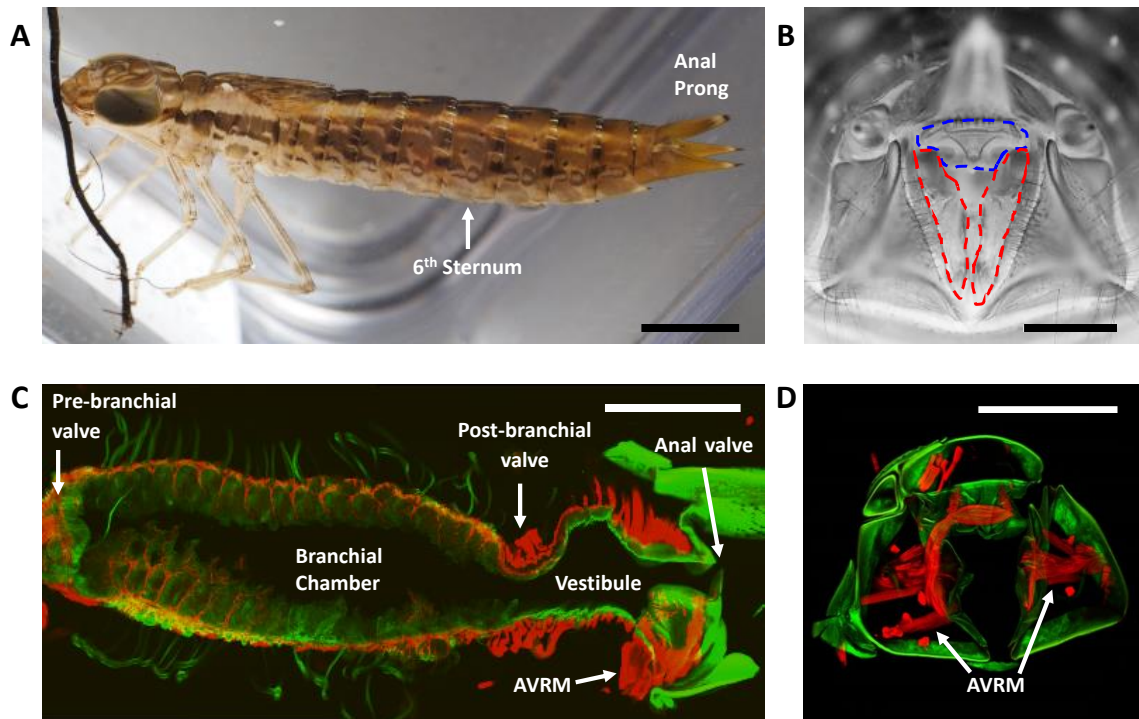


Figure 2.1. External and internal morphology of dragonfly larvae. AVR = anal valve retractor muscle. (A) Dragonfly larva *Anax* sp. The hindgut is located in the posterior half of the abdomen. Scale bar = 5 mm. (B) Tri-leaflet anal valve. The blue and red dotted lines trace the top leaflet and the bottom two leaflets, respectively. Scale bar = 1 mm. (C) Confocal microscope image of a sagittal section of the hindgut chamber of the dragonfly larvae. Red shows rhodamine-conjugated phalloidin staining of actin (muscle). Green shows calcofluor white staining of chitin (exoskeleton). Scale bar = 1 mm. (D) Confocal microscope image of a transverse section near the anal valve. Scale bar = 1 mm.

2.3.2 Flow visualization

The flow visualizations of respiration and jet propulsion are shown in figure 2.2. The larvae's respiratory jet is laminar. Owing to the periodic nature of the jetting, the vortex rollup is repeatedly observed. At times, the jet flow changes direction even though the abdomen does not move. In such cases, two jets are visible (Figure 2.2 C). The propulsion jet is turbulent. Instead of one or two coherent vortices, many small eddies are present.

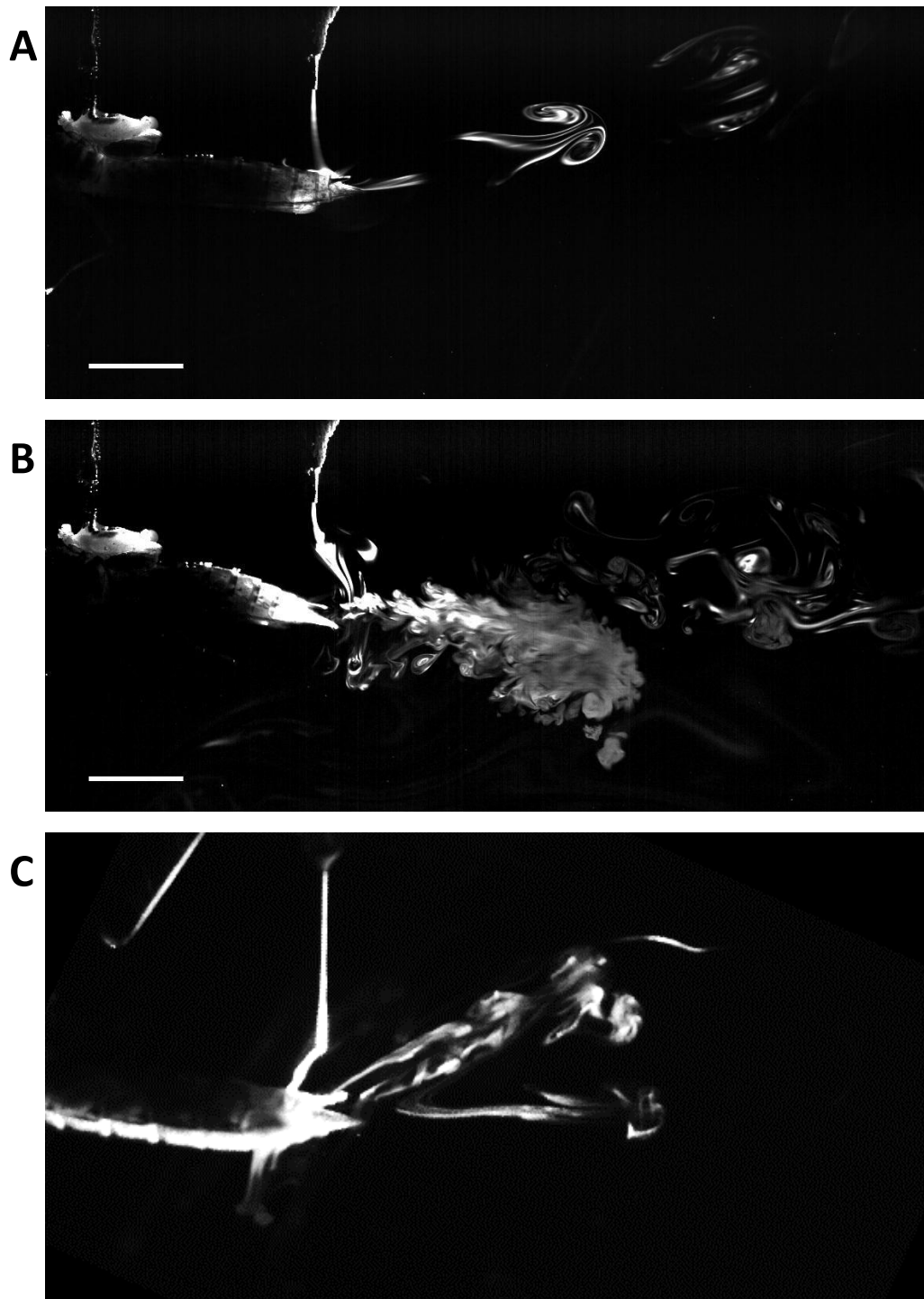


Figure 2.2. Flow Visualization of dragonfly larvae's ventilatory flow. (A) Respiratory flow visualization with Rhodamine 6G. Scale bar = 1 cm. (B) Jet propulsion flow visualization with Rhodamine 6G. Scale bar = 1cm. (C) Respiratory flow visualization with milk. Notice the two different jet directions.

2.3.3 Flow parameters

The respiratory jet speed approximated based on the particle streakline length was between 0.1 and $0.2 \text{ m}\cdot\text{s}^{-1}$ (Figure 2.3A). The respiratory jetting period, T , is about 1 s . Anal valve diameter is approximately $5 \times 10^{-4} \text{ m}$ (Figure 4.6F) and the kinematic viscosity of water is $\nu = 1 \times 10^{-6} \text{ m}^2\cdot\text{s}^{-1}$. Re based on these measurements is approximately 50 to 100 and \hat{T} is approximately 200 to 400 .

The propulsion mode jet speed measured based on the length of a streakline was 1 to $2 \text{ m}\cdot\text{s}^{-1}$ (Figure 2.3B). The propulsion jetting period, T , is about 0.1 s . Anal valve diameter is approximately $4 \times 10^{-4} \text{ m}$ (Figure 4.6C). Re based on these measurements is approximately 400 to 800 , and \hat{T} is approximately 250 to 500 .

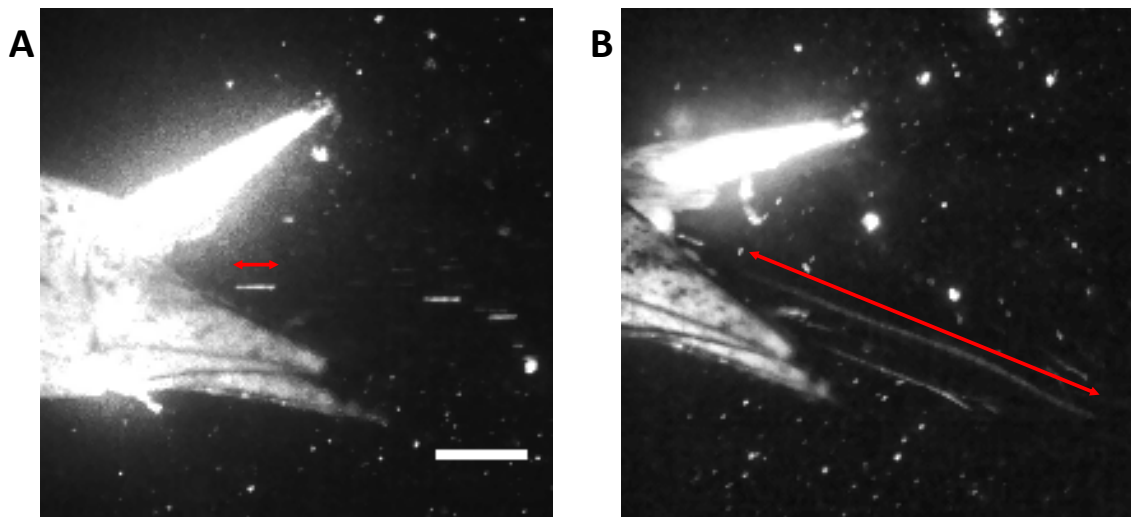


Figure 2.3. Particle pathline. (A) Respiratory flow particle pathline. The white streak corresponds to 22 cm/s . Scale bar = 1 mm (B) Jet propulsion flow particle pathline. The white streak corresponds to 2 m/s .

2.4 Discussion

2.4.1 Valves

The anal valve is morphologically different from the other two valves. The valve is composed of three leaflets with individually connected anal valve retractor muscles (AVRM). With AVRM, the leaflets can be retracted independent of each other. Such leaflet motion and its impact on the fluid flow will be discussed in chapter 4.

2.4.2 Flow Visualization and Reynolds number

The flow visualization shows that the dragonfly larvae's jet shifts from laminar to turbulent jet with the change of the ventilatory mode. This transition is a Reynolds number dependent phenomenon. The transition for the jet flow occurs at a critical Re of $O(1000)$. The respiratory jet is well below this critical Re , while the Re of the propulsion jet is close to the critical Re . Thus, the observed transition seems reasonable.

The flow visualization also revealed that the respiratory jets could emerge in various directions (Figure 2.2C). The dragonfly larvae's jet vectoring mechanism appears to be different from other biological jetters. The jet vectoring in other organisms, such as squid, is achieved by directing the jet exit at the desired angle. However, the dragonfly larvae's jet vectoring is achieved while the abdomen remains still. Their jet vectoring mechanism and potential biological benefit will be discussed in chapter 4.

2.4.3 Formation time

Previous studies have shown that thrust of pulsatile jetting could be enhanced by up to 50% by staying close to a formation time of 4 (Krueger and Gharib, 2003, 2005). In the case of dragonfly larvae's jetting, the formation time is about two orders of magnitude larger

than the critical formation time. Therefore, the effects of vortex rollup seems negligible.

This idea will be revisited briefly in chapter 3.

CHAPTER 3: Forces involved in reciprocal jetting of dragonfly larvae

3.1 Objectives

In this chapter, the dominant forces in dragonfly larvae's reciprocal jetting are identified through the comparison of direct force measurement and hydrodynamic forces calculated from the dragonfly larvae's abdominal movement and anal valve opening size.

3.2 Materials and Methods

3.2.1 Animal collection and care

Dragonfly larvae of family Aeshnidae were obtained from Ward Science (West Henrietta, NY, USA). Genus and species were not identified, but the batch included genera *Aeshna* and *Anax*. The morphology and previously measured flow parameters between these two genera were similar (Hughes and Mill, 1966). Thus, variation within the family Aeshnidae was expected to be small. The larvae were not sexed. The larvae were maintained at room temperature in an aquarium. The aquarium was covered with a black cloth at all times except during feeding to discourage the larvae from cannibalism. The larvae were fed commercially available small crickets, flightless fruit flies, or mealworms (PetSmart, Pasadena, CA, USA) 3–4 times/week.

3.2.2 Experimental setup and procedure

The overall setup is shown in the figure 3.1. The experiment was conducted in a clear acrylic water tank with dimensions of 20.955 cm (w) \times 8.89 cm (l) \times 12.7 cm (h). Water was filled up to 9.5 cm, and a dragonfly larva was placed approximately 7 cm below the water surface. The experimental protocol was as follows: dragonfly larvae were dried and tethered onto a metal rod by using dental wax. The metal rod was then attached to a single-axis force

sensor (SI-KG2B; WPI Inc., Sarasota, FL, USA). Water temperature was maintained at room temperature. The larvae were assimilated to the environment for 10 min before data collection. Same setup and procedure were used for the measurements in chapter 4.

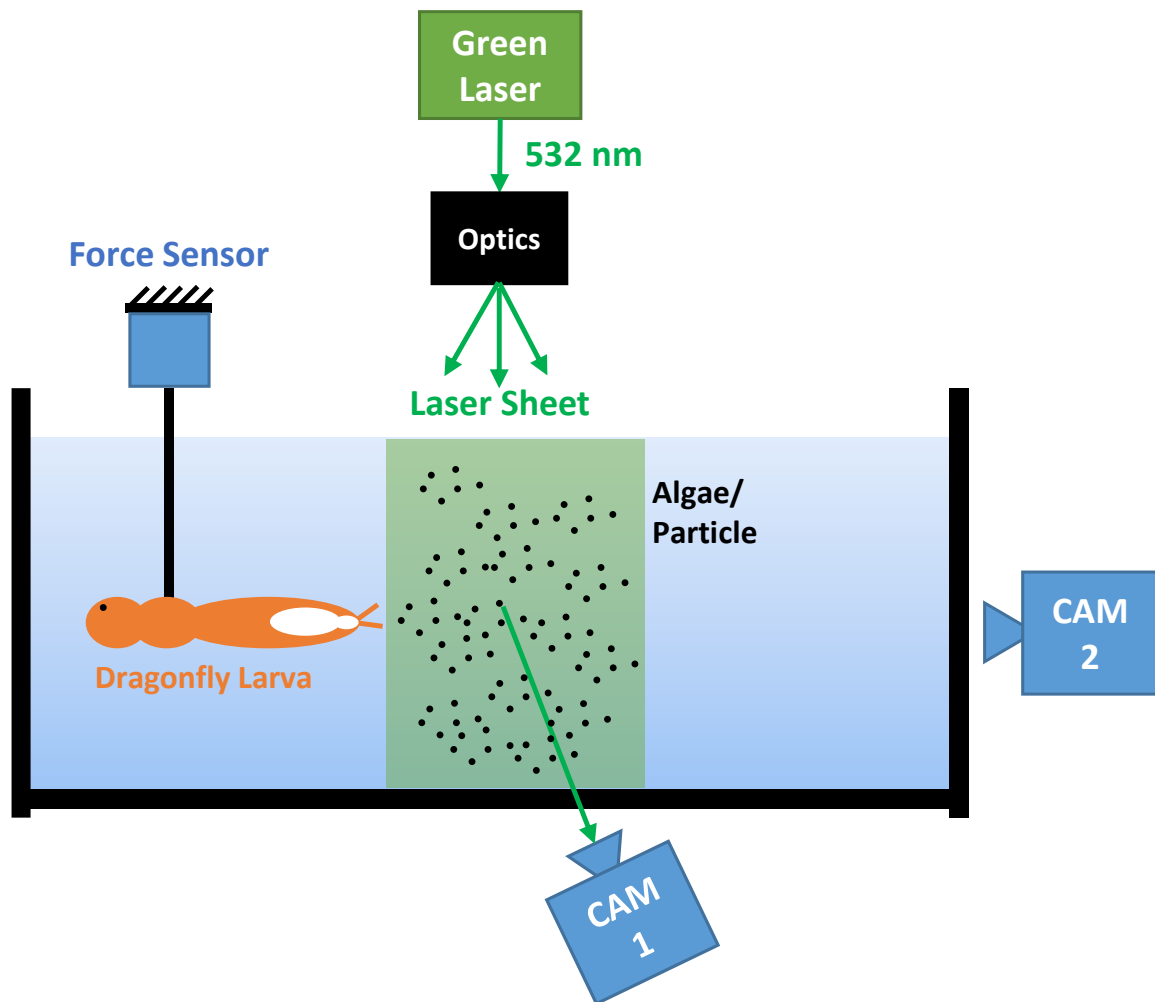


Figure 3.1 Schematic of the experimental setup. Dragonfly larva is tethered onto a single-axis force sensor. Water is pre-seeded with algae or 20- μm glass particles. Camera 1 images body kinematics and particle movements outside the chamber. Camera 2 images anal valve movements. The measurements are all synchronized.

3.2.3 Force measurement

The force generated by the tethered larvae was collected at 10,000 Hz. The thrust measurement was filtered using a zero-phase-lag digital filtering function, ‘filtfilt’, on Matlab 2014a (Mathworks, Natick, MA, USA). The cut-off frequency was set at 10 Hz, which is about half of the dominant noise frequency.

The effect of tethering for the respiratory study was expected to be small since the larvae naturally remain immobile during breathing. However, the nature of jet propulsion is a high-speed escape. Therefore, tethering inevitably ignores co-flow effect, added mass effect, form drag, and viscous drag. Co-flow can potentially reduce the measured thrust; the other three would affect the net force on the larvae, but have minimal impact on the measured jetting force. The details on how to calculate these values are provided in the discussion section (3.4.3).

3.2.4 Abdominal kinematics and volumetric flow rate scaling

For respiration, dorsoventral contraction and relaxation were measured as the time varying height of the sixth sternum (Figure 2.1A, white arrow). The laser sheet illuminated the abdomen of the larvae. High-speed camera (Figure 3.1; Camera 1, Dantec NanoSense Mk-III; Skovlunde, Denmark; 105 mm Sigma Lens; Ronkonkoma, NY, USA) recorded the movement along with the flow measurement. The intensity of the image along the sixth sternum was tracked using ‘StackProfile’ function in ImageJ. A custom Matlab code was used to determine the location of a sharp gradient of intensity.

For jet propulsion, longitudinal contraction and relaxation were measured by tracking the tip of the anal prong. The tip of the anal prong was tracked manually by using ImageJ. The measurement of the dorsoventral contraction for the jet propulsion mode was rendered

difficult to take by the longitudinal contraction of the abdomen, which moved the sternum out of the recording frame.

The first derivative of the measured sternum movement and longitudinal contraction were differentiated using the center difference method. Before the differentiation, the noise was filtered using a ‘smooth’ function from Matlab with a span of 5% of the full duration of the ventilation cycle. The second derivative was obtained in the same way.

Because respiratory contraction involves change in one dimension, the volume change scales with the height change, i.e. $Q=dV/dt \propto dh/dt$, where Q is the volumetric flow rate, V is the volume, and h is the height of the abdomen. During jet propulsion, the larvae contract their abdomens in two dimensions, both in the longitudinal and dorsoventral directions. Therefore, $Q \propto (dh/dt * z + h * dz/dt)$, where z is the longitudinal length, and h is the height of the sternum. However, assuming dh/dt is small based on Hughes (1958), the relation simplifies to $Q \propto dz/dt$.

3.2.5 Fluid Model

A fluid model developed by Krieg and Mohseni (2015) describes hydrodynamic forces associated with the fluid flowing in and out of the deformable cavity. The same model was used to analyze the jetting and refilling of dragonfly larvae. In the model, pressure is correlated to jet exit area and volume flux as follows:

$$P_b - P_\infty = C_1 \frac{Q^2}{A^2} + C_2 \frac{d\left(\frac{Q}{R}\right)}{dt} \quad (3.1).$$

Here, P_b is the reference pressure at the apex of the chamber, P_∞ is the ambient pressure, A is the area of the nozzle, R is the radius of the nozzle, Q is the volumetric flow rate, and C_1 and C_2 are constants.

Equation (2.1) was derived by Krieg and Mohseni (2015) through integrating the momentum equation along the line where the viscous effect is small. The first term on the right hand side of the equation (2.1) describes pressurization of the chamber owing to the momentum flux out of the chamber. This term will be referred to as quasi-steady flux term. For an unsteady pulsatile jetting with formation time close to 4, the over-pressurization by vortex ring roll up is significant (Dabiri, 2009; Krueger and Gharib, 2003, 2005). For the respiratory and propulsion flow of dragonfly larvae, the over-pressurization effect is neglected on the basis that each jetting phase is relatively long, indicated by a large formation time (section 2.4.3).

The second term on the right hand side of the equation (3.1) describes pressurization of the chamber owing to the unsteady acceleration of the fluid. This term is called the half-sink term, because it was calculated using the half-sink flow (Krieg and Mohseni, 2013, 2015). Herein, we assumed that the reference pressure remains uniform throughout the chamber. With this assumption, force and power related to the pressure are given as follows:

$$T = \Delta P_b A = C_1 \frac{Q^2}{A} + C_2 A \frac{d\left(\frac{Q}{R}\right)}{dt} \quad (3.2),$$

$$P_o = \Delta P_b Q = C_1 \frac{Q^3}{A^2} + C_2 Q \frac{d\left(\frac{Q}{R}\right)}{dt} \quad (3.3),$$

where T is thrust, and P_o is power. These equations describe both the jetting and refilling phases.

The usefulness of the equation (3.2) is that the forces are related to the abdominal kinematics and the orifice size. In addition, thrust is decomposed into the quasi-steady flux

term and the unsteady acceleration term. Therefore, comparing each term with the direct force measurement can show their relative importance at any given time.

3.2.6 Finding C_1 and C_2

To calculate C_1 , a time point where $d^2h/dt^2=0$ or $d^2z/dt^2=0$ was selected (marker ‘o’ in Figure 3.3). Then the corresponding quasi-steady flux term value was divided by the corresponding thrust value. To calculate C_2 , a time point where $dh/dt=0$ or $dz/dt=0$ was selected (marker ‘*’ in Figure 3.3). Then the corresponding half-sink term value was divided by the corresponding thrust value.

3.2.7 Area of anal orifice

Area of anal orifice was recorded with Camera 2 (Figure 3.1, IMPERX 210P; Boca Raton, FL, USA; 90 mm Tamron Lens; Saitama, Japan, or Olympus OMD-EM-1; Tokyo, Japan). The orifice area varies from jetting phase to refilling phase. However, variation within phases is small. Therefore, the orifice area is assumed to be constant during each phase, and transition is assumed to occur linearly. The ratios of jetting and refilling orifice size are reported in table 2.

3.2.8 Experiment summary table

Four comparison cases (Table 1) are considered. The four cases compare different parts of equation (3.2). These cases are tested in five ventilation cycles of which three were respiratory cycles and one was jet propulsion cycle (Table 2). The three respiratory cycles vary in their sternum position curve shape (Figure 3.3) and in their ventilation period. Hereafter, they will be referred to as case 1, 2, 3, 4 and ventilation 1, 2, 3, 4.

	Title	Model	Equation #
Case 1	Quasi steady	$T = \frac{Q^2}{A}$	(3.4)
Case 2	Half-sink	$T = C_2 A \frac{d\left(\frac{Q}{R}\right)}{dt}$	(3.5)
Case 3	Quasi steady + Half sink	$T = C_1 \frac{Q^2}{A} + C_2 A \frac{d\left(\frac{Q}{R}\right)}{dt}$	(3.6)
Case 4	Neglect flux term during refilling	$T = \begin{cases} C_1 \frac{Q^2}{A} + C_2 A \frac{d\left(\frac{Q}{R}\right)}{dt} & t = time_{jet} \\ C_2 A \frac{d\left(\frac{Q}{R}\right)}{dt} & t = time_{refill} \end{cases}$	(3.7)

Table 3.1 Tested four variations of equation (3.2).

	Mode	Period (s)	Jetting	Refilling	Area Ratio
Ventilation 1	Respiration	3.88	Convex	Concave	0.206
Ventilation 2	Respiration	2.13	Convex	Concave	0.674
Ventilation 3	Respiration	3.63	Convex	Convex	0.277
Ventilation 4	Jet Propulsion	0.33	Concave	Convex	0.133

Table 3.2 Tested four ventilation cycles.

3.3 Results

3.3.1 Force measurements

The force measurement of three respiratory cycles are shown in figure 3.2A-C. The force measurement shows a gradual increase in force followed by a sharp transition to the negative thrust. Jet propulsion force measurement is shown in figure 3.2D. The magnitude

of the force measured for jet propulsion is about 2-3 orders of magnitude larger than during respiration.

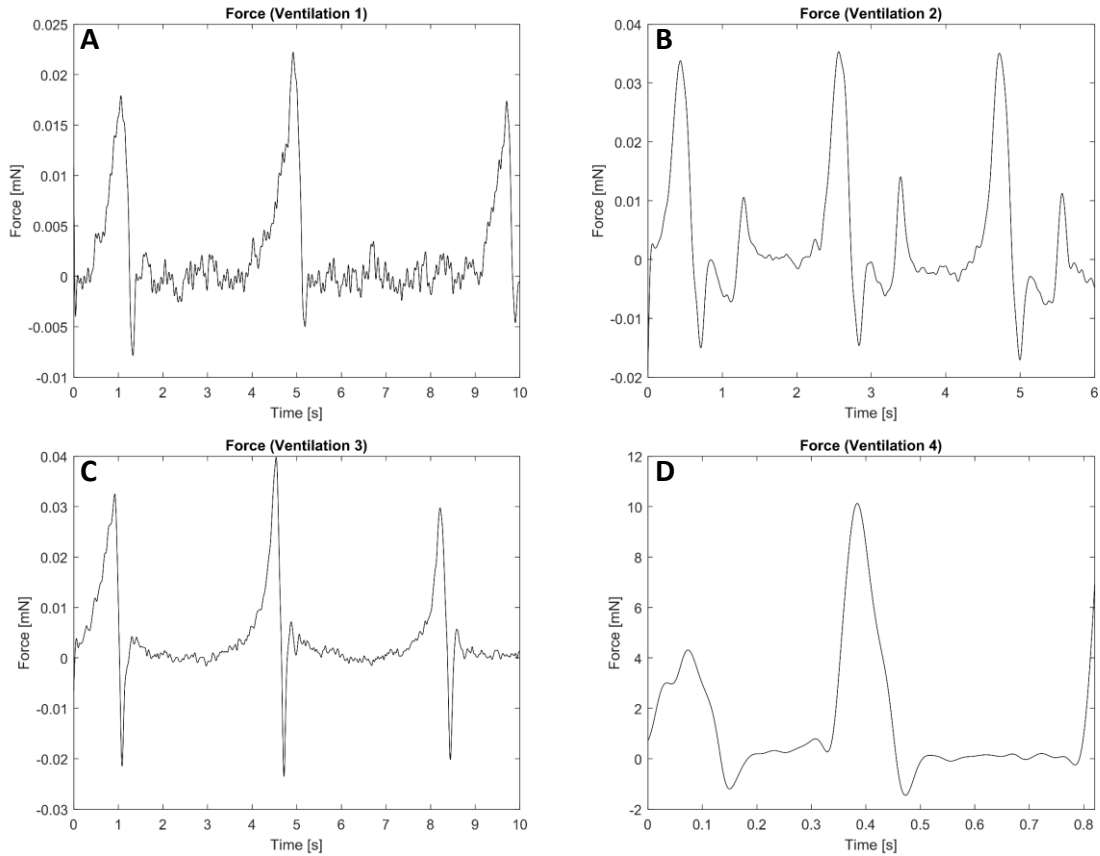


Figure 3.2 Force measurements. (A) Ventilation 1. (B) Ventilation 2. (C) Ventilation 3. (D) Ventilation 4.

3.3.2 Abdominal kinematics

Figure 3.2A-C shows the sternum position curves of the three different respiratory cycles and their first and second time derivatives (note the concavity of the sternum position curve, which is summarized in table 2). Figure 3.2D shows the longitudinal length change curve of the jet propulsion and its first and second time derivatives.

The first derivative curve provides a reliable way of distinguishing the jetting phase from the refilling phase. Jetting and refilling phases are defined as time when the first derivative is positive and negative, respectively.

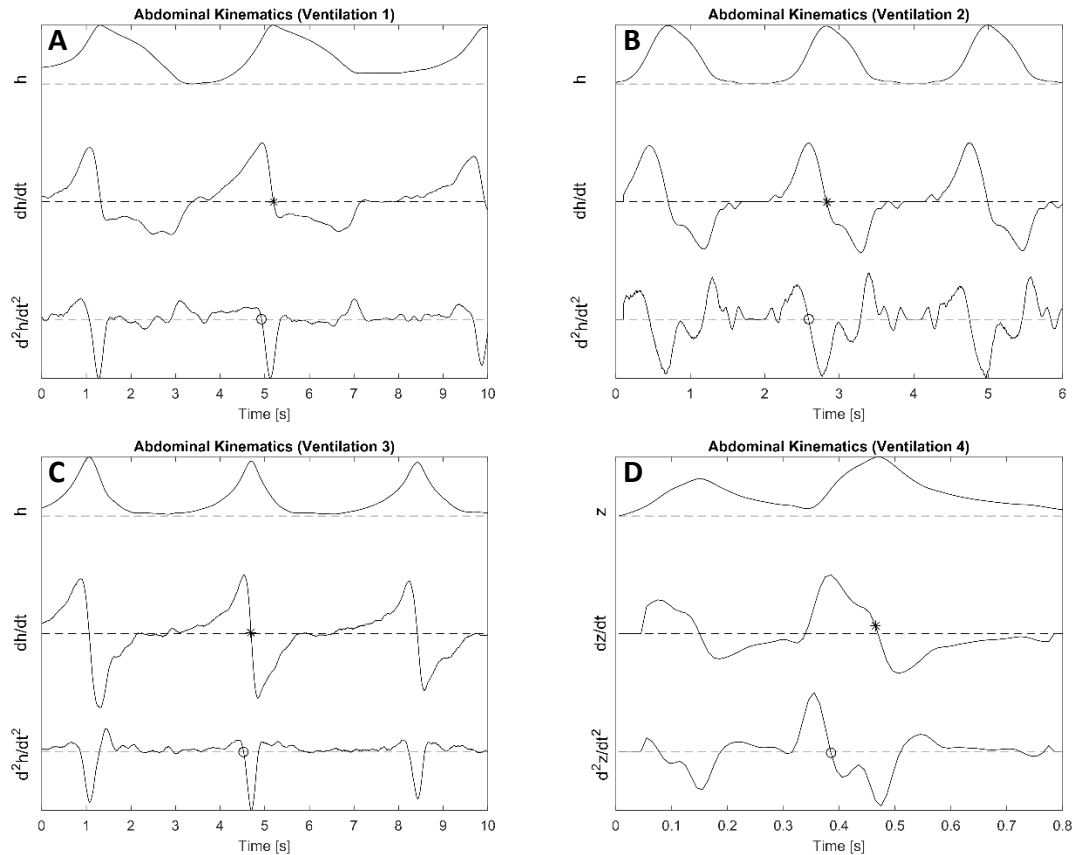


Figure 3.3 Abdominal kinematics and derivatives. ‘*’ is where dh/dt or $dz/dt = 0$. ‘o’ is where $d^2h/dt^2=0$ or $d^2z/dt^2 = 0$. Curves are normalized with their maximum values. (A-C) Ventilation 1-3; Position of 6th sternum and its derivatives. (D) Ventilation 4; Longitudinal length change.

3.3.3 Force and volume comparison

Figure 3.4 shows case 1 comparison, in which the quasi-steady flux term is considered. In all four ventilation cycles, the flux term closely follows the force curve during the jetting phase. However, this is not the case during the refilling phase. Specifically, the negative peaks in ventilation 1 are not traced by the flux term. Furthermore, instead of the

fluctuating force measurement seen in ventilation 2, the trend of the flux term has one negative peak.

Figure 3.5 shows case 2 comparison, in which the half sink term is considered. In all four ventilation cycles, the half-sink term closely follows the force curve during the refilling phase. The negative peaks in ventilation 1, 3, and 4, as well as the fluctuating force in ventilation 2 are traced well by the half-sink term. For all four ventilations positive peaks near the start of the jetting phase is observed, but the magnitude is much lower than the measured force.

Figure 3.6 shows case 3 comparison, in which both quasi-steady and half-sink terms are considered. The addition of the two terms traces the force curve well for the ventilation 1. However, for the ventilation cycles 2, 3 and 4, there is noticeable deviation from the force curve.

Figure 3.7 shows case 4 comparison, in which the quasi-steady term is neglected for the refilling phase. A selective addition of the two terms appears to trace the force curve well for all five ventilation cycles.

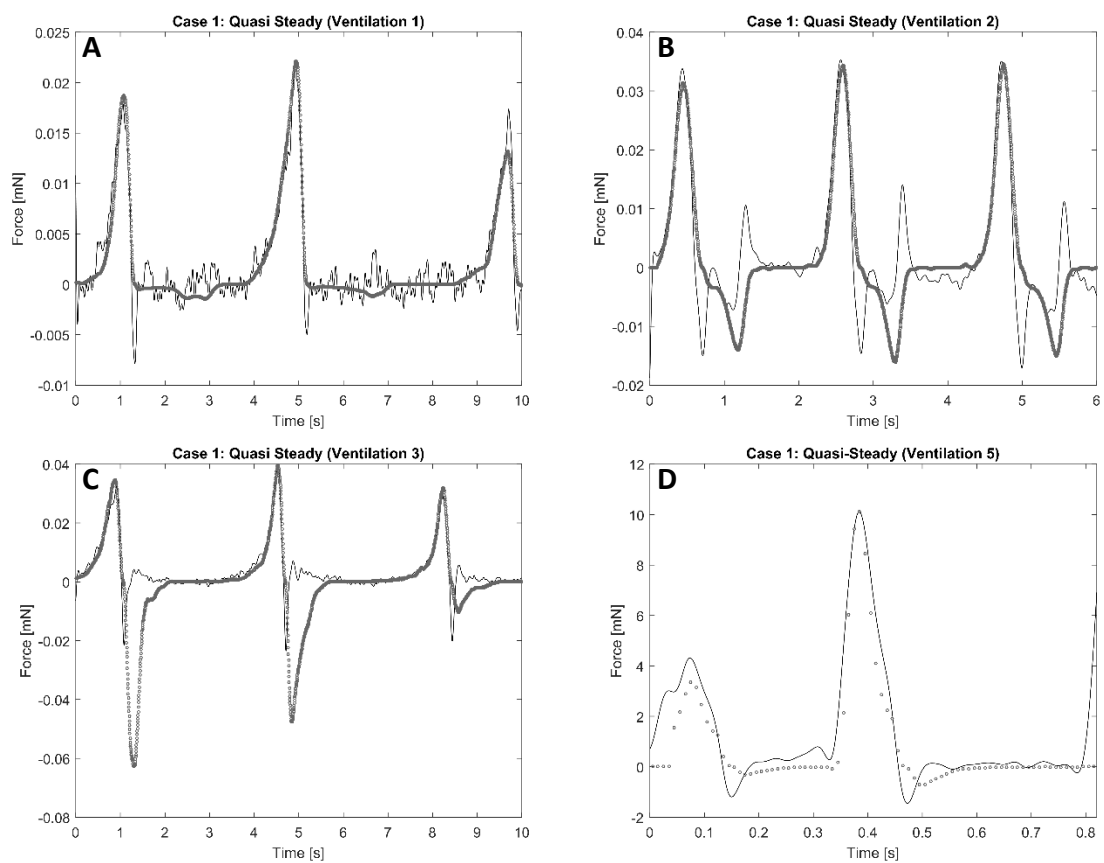


Figure 3.4 Case 1. Black line is the force measurement. Grey circles are the result of equation 3.4. (A) Ventilation 1. (B) Ventilation 2. (C) Ventilation 3. (D) Ventilation 4.

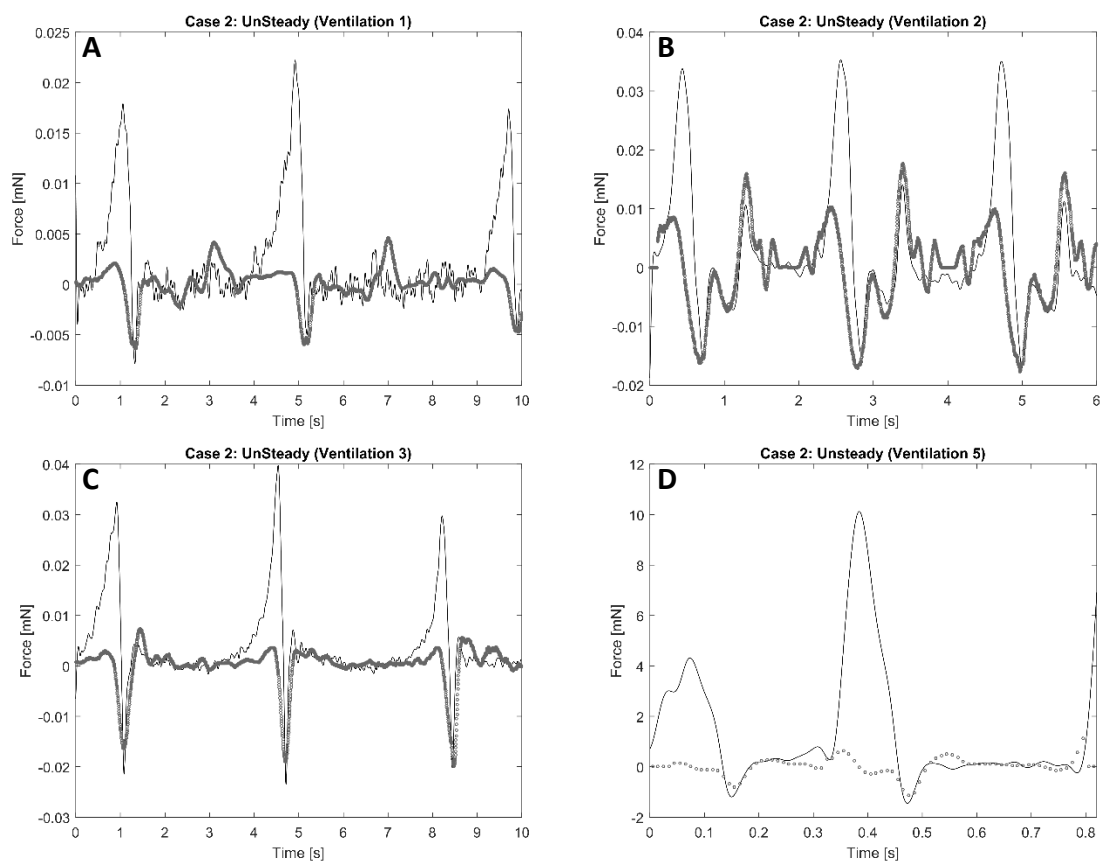


Figure 3.5 Case 2. Black line is the force measurement. Grey circles are the result of equation 3.5. (A) Ventilation 1. (B) Ventilation 2. (C) Ventilation 3. (D) Ventilation 4.

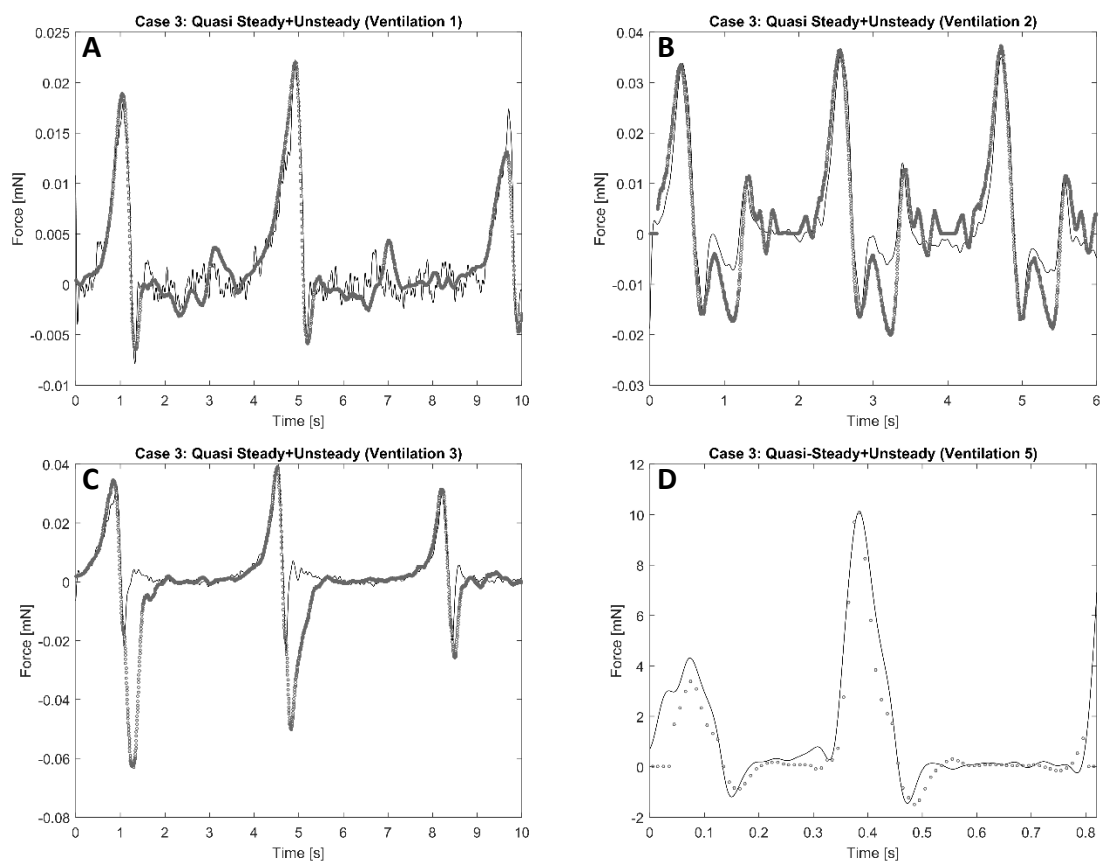


Figure 3.6 Case 3. Black line is the force measurement. Grey circles are the result of equation 3.6. (A) Ventilation 1. (B) Ventilation 2. (C) Ventilation 3. (D) Ventilation 4.

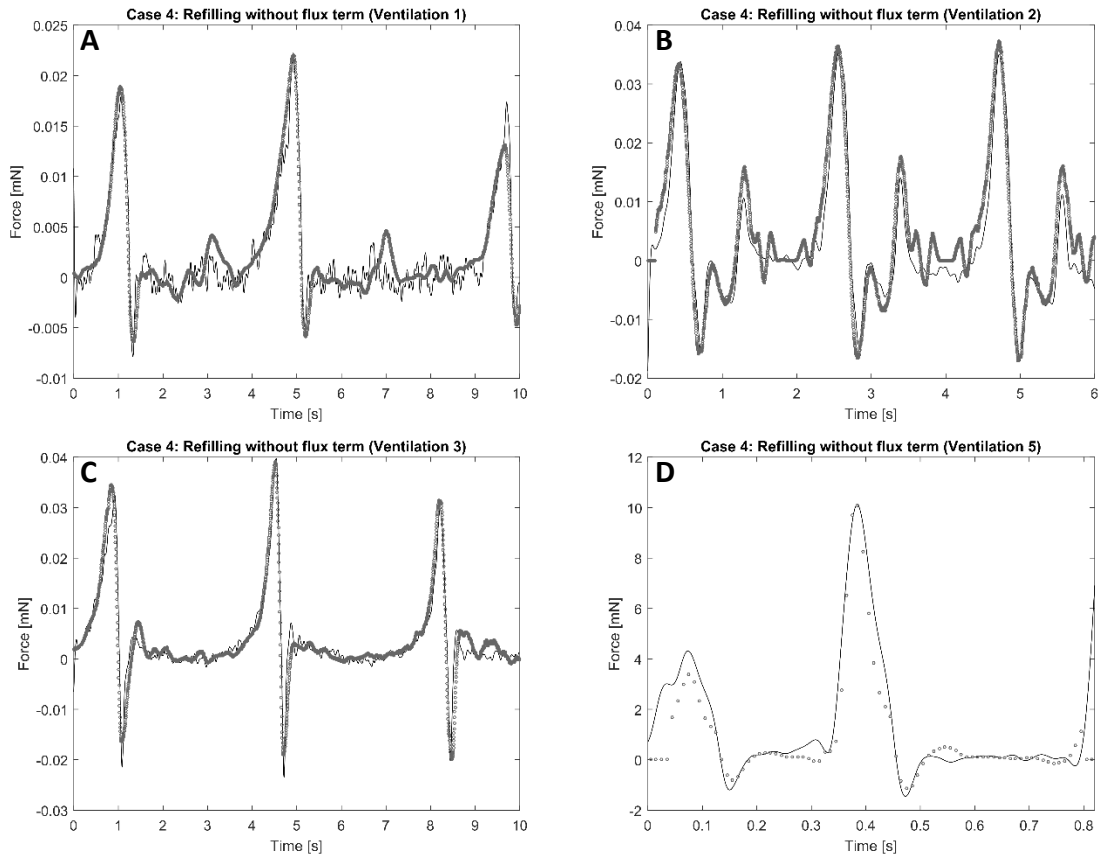


Figure 3.7 Case 4. Black line is the force measurement. Grey circles are the result of equation 3.7. (A) Ventilation 1. (B) Ventilation 2. (C) Ventilation 3. (D) Ventilation 4.

3.3.4 Impulse generated during jet propulsion

Figure 3.8A shows the impulse integrated from jet propulsion thrust measurement. Figure 3.8B solid black line shows the impulse integrated from hydrodynamic force calculated from equation (3.7). The two results are qualitatively similar. In figure 3.8B, the contribution of the unsteady half-sink and quasi-steady flux term are plotted separately. The line connecting the start of the ventilation cycle to the start of the next ventilation cycle is also plotted. The slope of this line represents the average thrust during that cycle.

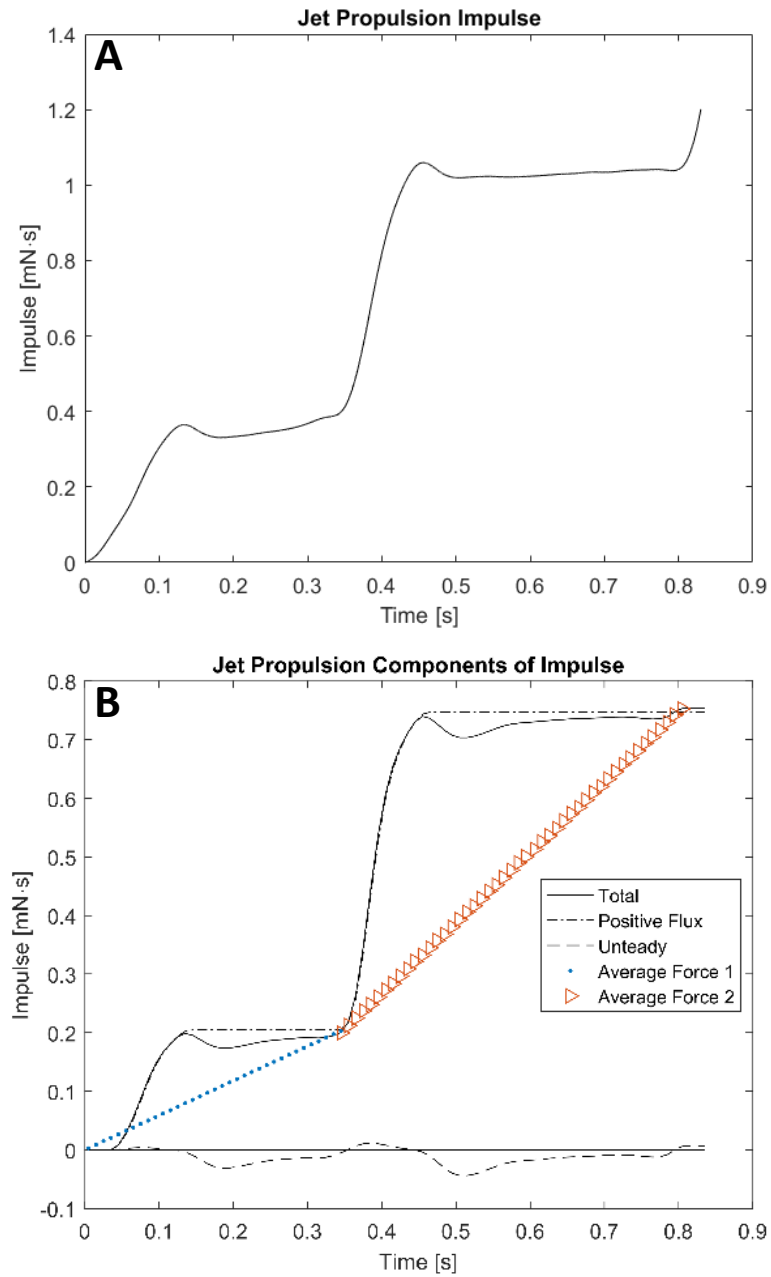


Figure 3.8 Jet propulsion impulse. (A) Impulse integrated from the force measurement. (B) Impulse integrated from equation (3.7).

3.4 Discussion

3.4.1 Dominant forces during jetting and refilling phases.

Cases 1 and 2 shows that the respective dominant forces during the jetting and refilling phases are the quasi-steady flux term and unsteady half-sink term. Furthermore, the comparison of cases 3 and 4 shows that the unsteady half-sink term is not just the dominant term, but also the only term that contributes to the measured force. This is evident from ventilations 2 and 3, which clearly show that large negative volumetric flux does not contribute to the thrust.

The reason that the quasi-steady flux term has no contribution during the refilling phase is explained as follows. At the end of the jetting phase, the branchial chamber of the dragonfly larvae almost completely collapses, losing approximately 85% of the volume (Hughes and Mill, 1966). Therefore, the negative thrust due to the flux of momentum entering the chamber is cancelled out by the positive thrust due to the immediate impingement of the fluid at the chamber wall. In other words, the force associated with quasi-steady flux term is an internal force.

On the other hand, the half-sink term is not zero during the jetting phase, despite the quasi-steady term's dominance. Near the end of the jetting phase, the half-sink curve has a prominent negative peak. This peak shows up because the fluid flowing out needs to be reversed before the refilling begins. Another time when the half-sink curve has a prominent peak is near the beginning of the jetting phase of the propulsion. A positive peak shows up because of the sudden acceleration of the fluid inside the chamber.

3.4.2 Impulse generated during Jet propulsion

The impulse of the jet propulsion shows that the larvae gains momentum during the jetting phase. The net contribution of the unsteady half-sink term to the impulse is zero when one full cycle is considered. A similar result was shown in the experiment by Krieg and Mohseni (2015).

Thus, during the jetting phase, fast expulsion of fluid would mean more contribution to the total impulse. On the other hand, during the refilling phase, the net impulse is zero regardless of how fast the chamber is refilled. Fast refilling, however, would increase the average thrust. The average thrust is equal to the slope of the straight line connecting the start of the ventilation cycle and the start of the next ventilation cycle. As the refilling time decreases, the slope gets steeper indicating a larger average thrust.

3.4.3 Effect of tethering

The force and impulse measurements are made on the tethered dragonfly larvae. While this is a good representation of the respiratory jet, the purpose of propulsion is to move, and therefore the discrepancy between tethered and free-swimming dragonfly larvae is considered here.

Free-swimming dragonfly larvae are subjected to co-flow effect and drag. Co-flow is the flow around the swimming larvae. The vortex ring pinches off earlier in the presence of co-flow flowing in the same direction as the jet (Krueger et al., 2003, 2006). An early pinch-off can limit thrust enhancement by over-pressurization. The co-flow effect is significant when the ratio between co-flow and average wake velocity is greater than 0.5. The maximum swimming velocity and jet speed are approximately 50 cm/s and 2m/s, respectively. Since the velocity ratio is less than 0.5, the co-flow effect on the vortex ring

formation is expected to be small. In any case, the high formation time indicates that the overall effect of vortex roll-up would be small.

Drag force slows down the larvae by acting in the opposite direction of their motion. The drag force can be divided into three different components: added mass, form drag, and viscous drag. These forces are included in the integral of stress tensor around the insect body as $\int_{\text{Body}} (-p\mathbf{I} + \mu(\nabla\mathbf{u} + (\nabla\mathbf{u})^T)) \cdot \mathbf{n} dS$, where p is pressure, \mathbf{I} is identity matrix, μ is dynamic viscosity and $\nabla\mathbf{u}$ is velocity gradient tensor, and \mathbf{n} is the outer normal from body. With a thin boundary layer approximation, we can assume that the pressure outside the boundary layer is equal to pressure on the surface of the larvae. Outside the boundary layer, the flow is irrotational, and thus pressure can be determined using the unsteady Bernoulli equation: $\frac{p}{\rho} = \frac{\partial\phi}{\partial t} + \frac{1}{2}u^2$. The integral of the first term on the right hand side is the added mass effect. The integral of the second term is the form drag. The viscous drag is given by the integral of $\mu(\nabla\mathbf{u} + (\nabla\mathbf{u})^T)$. More detailed studies on the external flow effect have been considered for similar body shapes (Anderson et al., 2001; Daniel, 1983; Ruiz et al., 2011).

CHAPTER 4: Anal valve kinematics

4.1 Objectives

In this chapter, the effect of anal valve kinematics on the respiratory and propulsion flow of the dragonfly larvae is studied. The thrust and power equations from chapter 3 are used to explain why both respiration and jet propulsion modes might have a small aperture during the jetting phase and a large aperture during the refilling phase. Furthermore, the independent movement of the leaflets and its effect on the fluid flow is described. All the measurements from previous and current chapters are plotted together, aligned in time, to provide a holistic view of the ventilatory events.

4.2 Materials and Methods

See section 3.2.1 and figure 3.1 for the experimental setup.

4.2.1 Valve kinematics and quantification

Valve kinematics were measured using a camera facing the anal opening (Camera 2, IMPERX 210P; Boca Raton, FL, USA; 90 mm Tamron Lens; Saitama, Japan, or Olympus OMD-EM-1; Tokyo, Japan). The images were recorded at 30 or 100 frames per second. The image sequence was manually measured for the valve opening area; two length scales, L1 and L2; and degree of asymmetry by using ImageJ version 1.48 (National Institutes of Health, Bethesda, MD, USA). L1 is the vertical length of the top leaflet, and L2 is the length of the bottom two leaflets connected in the middle (Figure 4.6). The degree of asymmetry was defined as the distance between the center of the valve opening to that of the entire valve normalized by the radius of the entire valve. The center of the valve opening and the entire

valve were estimated based on the center of the vertical span, D1 and D2 (Figure 4.6). The measured distance was normalized by half of D2.

4.2.2 Flow visualization

Flow was visualized by illuminating pre-seeded particles with a 532nm continuous laser sheet (LCS-0532-TSG-00200-05; Laserglow, Toronto, ON, Canada and MGL-F-532; Optoengine, Midvale, UT, USA). High-speed camera collected flow data at 250 or 300 frames per second (Camera 1, Dantec NanoSense Mk-III; Skovlunde, Denmark; 105 mm Sigma Lens; Ronkonkoma, NY, USA).

The resulting images were used to obtain both pathline visualization and velocity field. Two different types of particles were used for the experiment. The first type was 20- μm glass beads with neutral density (Potters Inc., Malvern, PA, USA). Since these particles have high reflectance, they are suitable for pathline visualization of both jet propulsion and breathing. However, the larvae displayed aversion after a few minutes of exposure, indicated by more frequent jet propulsion and attempts to clean themselves with their legs.

The second type was algae and small debris collected from a local pond; the larvae displayed less aversion. The most abundant algae in the collected water were *Scenedesmus* sp. (Figure 4.1). The algae were approximately 20–40 μm in size. They are neutrally buoyant and enclose chlorophyll, which fluoresces under green light (Wu et al., 2013).

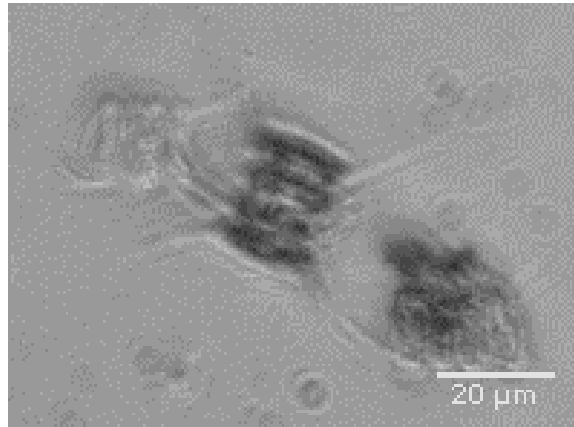


Figure 4.1 Green algae. *Scendesmus* sp.

4.2.2.1 Color-coded pathline visualization

A Lagrangian path of fluid flow can be produced experimentally by overlaying a particle image sequence onto a single image. This method is similar to pathline visualization by a long exposure, but it is more flexible in that it allows one to choose the range of time after the fact. It can also incorporate temporal information when a different color is assigned to an image at each time. The author termed this technique as a color-coded pathline. This pathline can be produced using the ‘Time-lapse Color Coder’ function of ImageJ.

4.2.2.2 Direction of the jet

The color-coded pathline visualization was used to manually measure the angle of the jet. 10–20 images were overlaid to produce the pathline image using ImageJ. The angle was measured with respect to the red reference line in figure 4.8B. The measured jet deflection angles were plotted with the degree of valve opening asymmetry corresponding to the same time. The respiratory flow direction and valve asymmetry were measured in six larvae (n=6; mean length=2.92 cm, s.d.=0.394 cm). The propulsion flow direction and valve asymmetry were measured in three larvae (n=3; mean length=2.42 cm, s.d.=0.246 cm).

4.2.2.3 Particle image velocimetry (PIV)

The PIV analysis was performed using the same raw images used in the color-coded pathline to produce a velocity field for each time interval. The images recorded at 250 frames·s⁻¹ with 3,997 ms exposure time were analyzed using commercially available software, PIVview2C (PIVtech, Göttingen, Germany), with the following parameters: image pair offset, 8; 32×32 pixel windows size; 16 pixel overlap; standard Fast Fourier Transform correlation; multi-pass interrogation; maximum displacement limit, 16 pixel; and median filter with 3×3 kernel size. The analyzed velocity field was used to plot the time variation of the velocity at a single point. The resulting time history plots were smoothed using a ‘smooth’ function in Matlab (Mathworks, Natick, MA, USA) with a span of 3. The flow measurement is valid up to approximately 5 mm/s—a velocity at which an object will move one pixel during the exposure time. Beyond this limit, the measurement is less accurate because the images suffer from motion blurring of the particles. This is an inherent problem when a continuous laser is used for particle image velocimetry. Nevertheless, flow field below 5 mm/s is a valuable tool for understanding slower fluid flow.

The entrainment flow velocity in the horizontal direction is in between 1-1.5 mm/s (Figure 4.2B), which is 1.6-2.4px/frame (conversion ratios=31.25 frames·s⁻¹ and 236.008px/4.74mm). The PIV algorithm employed has a subpixel accuracy and therefore, above-mentioned particle shift is measureable. The root mean square (RMS) of the residual was used to estimate the measurement error. The residual is defined as the moving average with interval of 3 subtracted from the raw data (Figure 4.2A). The computed RMS was 0.05 px/frames (0.03 mm/s).

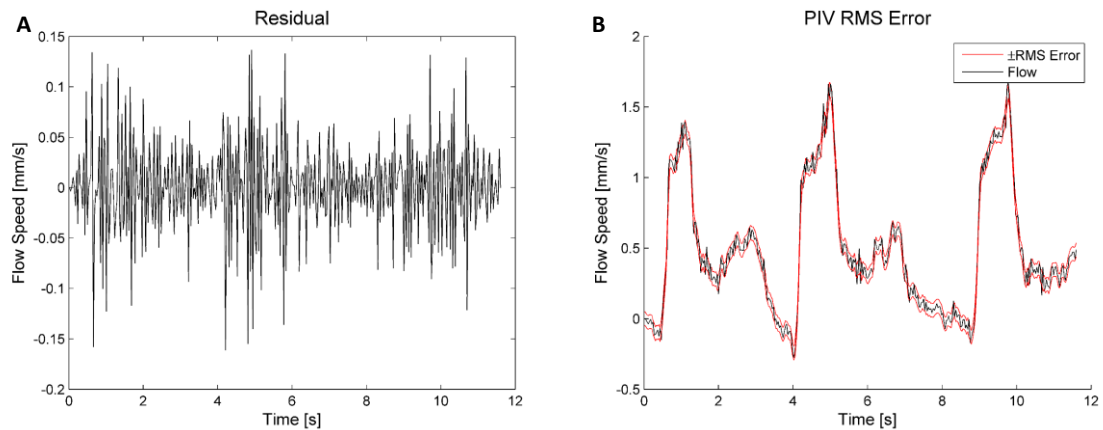


Figure 4.2 PIV error analysis. (A) Residual of the horizontal velocity. (B) ± 1 RMS error enveloping raw data.

4.3 Results

4.3.1 Anal valve kinematics

The change in anal orifice area over time for respiration is shown in figure 4.3A. Anal valve kinematics begins with the leaflets in a fully closed or slightly open position. During the jetting phase of respiration, the top leaflet is fully retracted, whereas the bottom two leaflets remain closed. The resulting valve opening is placed asymmetrically. During the transition to inhalation, all the three leaflets are retracted, thereby maximizing the valve opening area. At the end of the inhalation phase, the orifice is briefly closed. The exhalation anal orifice area to maximum aperture ratio varies from 1/2 to 1/5. The full sequence of the respiratory valve kinematics is shown in figure 4.4.

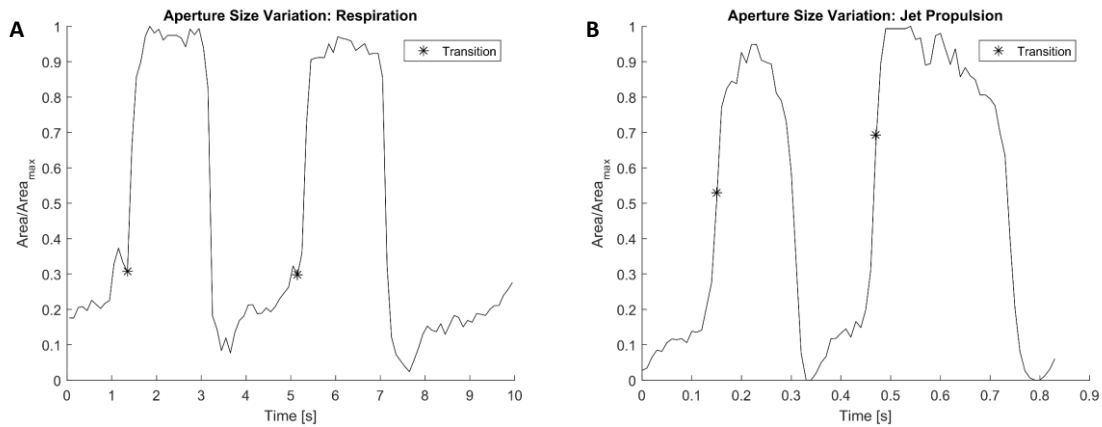


Figure 4.3 Area of anal opening. The curve is normalized with maximum value. ‘*’ marks transition from jetting to refilling phase. (A) Respiration. (B) Jet propulsion

The change in anal orifice area over time for jet propulsion is shown in Figure 4.3B. Anal valve kinematics of jet propulsion begin with a completely closed valve. During the jetting period, all three leaflets partially open to create a small opening (variation $1/4 \sim 1/8$ of maximum aperture). During the transition to the refilling phase, all three leaflets are completely retracted, maximizing the anal orifice area. The complete sequence of the valve kinematics is shown in figure 4.5.

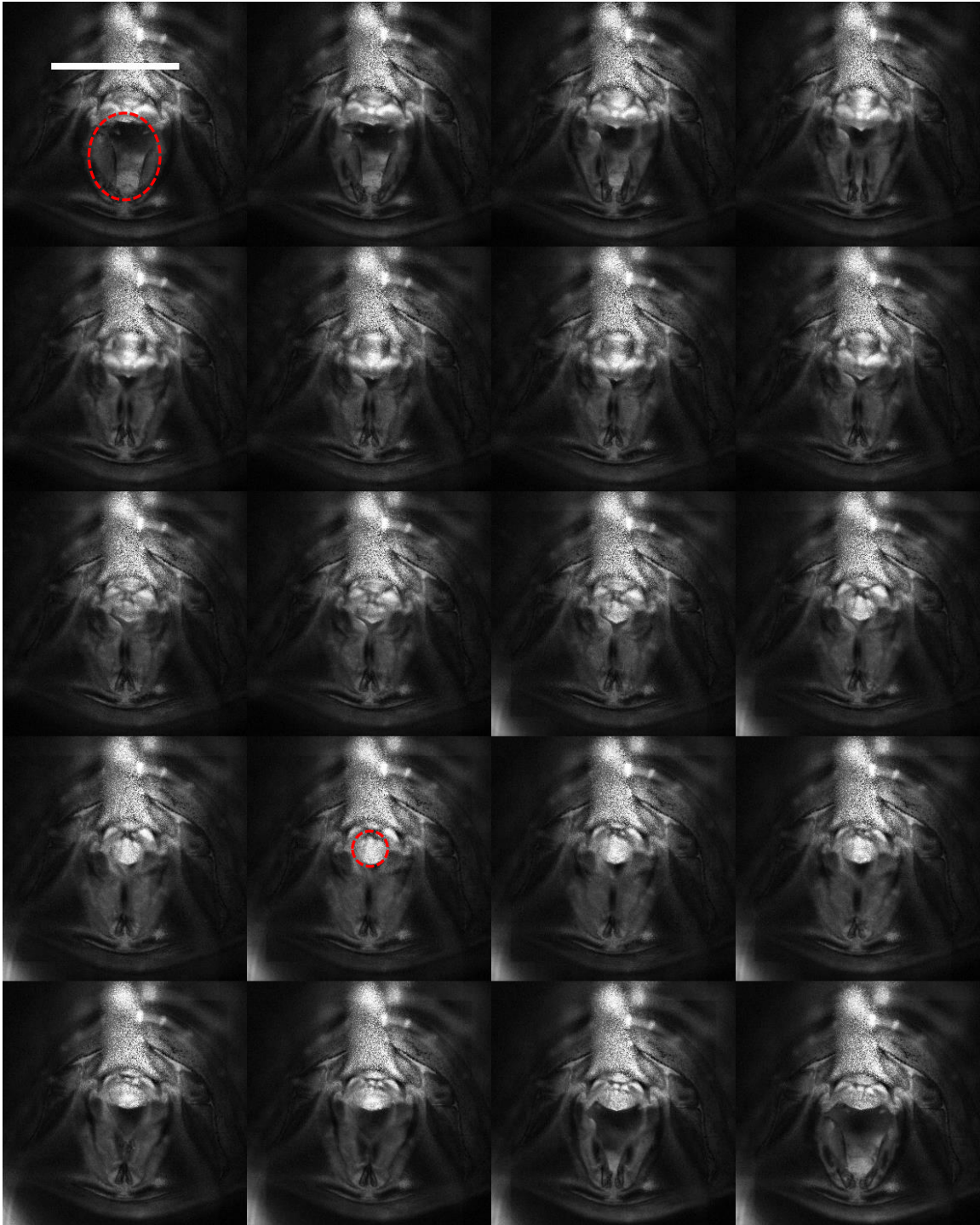


Figure 4.4 Full sequence of respiratory anal valve kinematics. Time interval between images=0.16 s, scale bar=2mm. Red lines trace valve opening. Time from left to right and top to bottom.

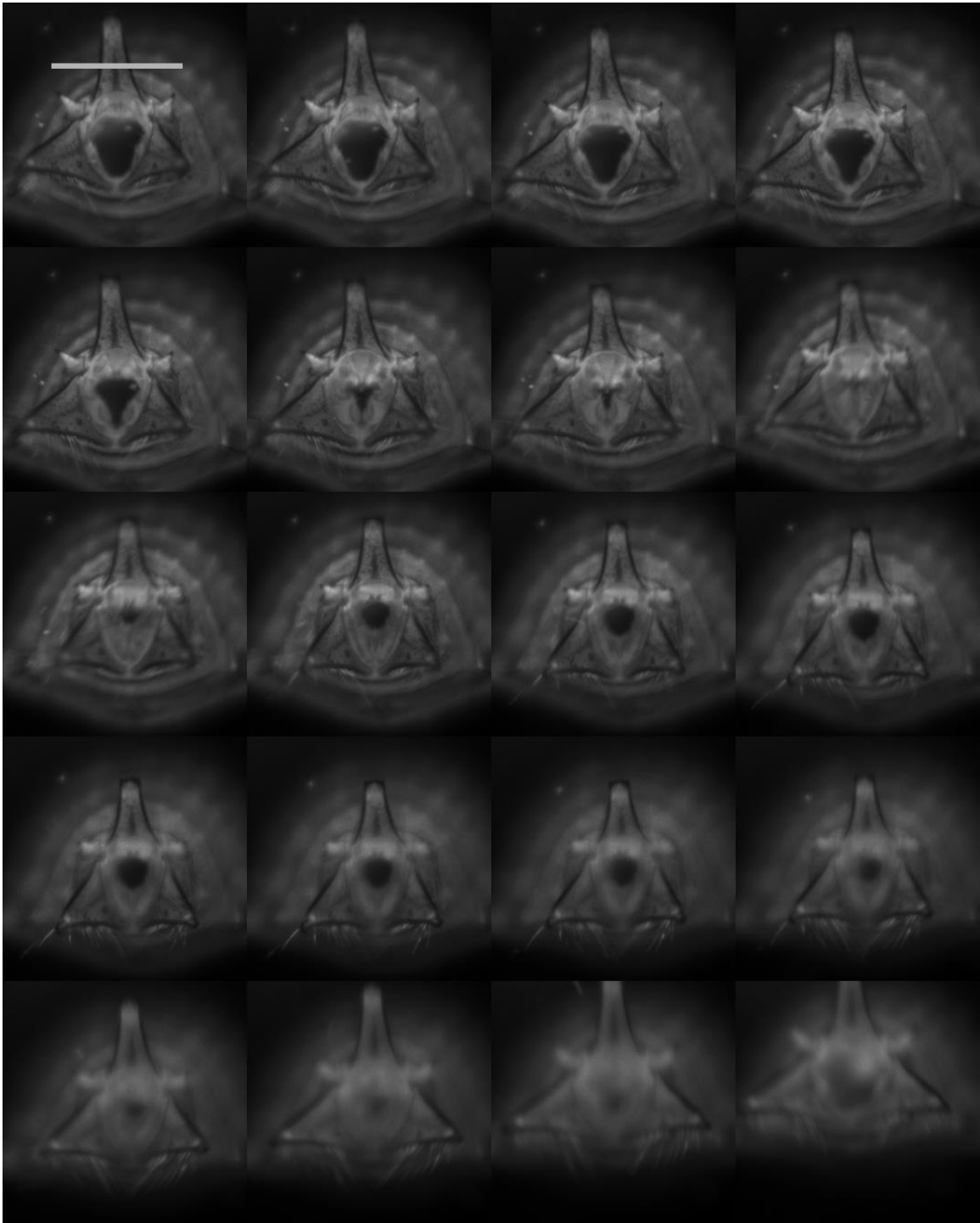


Figure 4.5 Full sequence of jet propulsion anal valve kinematics. Time interval between images=0.01 s, scale bar=2mm. Time from left to right and top to bottom.

4.3.2 *Quantifying asymmetric opening*

The time variation of the two additional length scales, L1 and L2 defined in section 4.2.1, were measured and plotted in figure 4.6. For the respiration mode, when the exit area widens at the start of the jetting phase (approximate time = 1.3 s), L1 is reduced, whereas L2 remains unchanged. The reduction in L1 signifies the retraction of the top leaflet. The unchanged L2 signifies closed bottom leaflets. For the propulsion mode, when the exit area widens at the start of the exhalation phase (approximate time = 0.09 s), L1 and L2 are both reduced. A reduction signifies the retraction of both the top and the bottom two leaflets. Thus, for the respiration, the resulting nozzle opening is placed away from the center, whereas for the jet propulsion, it opens near the center.

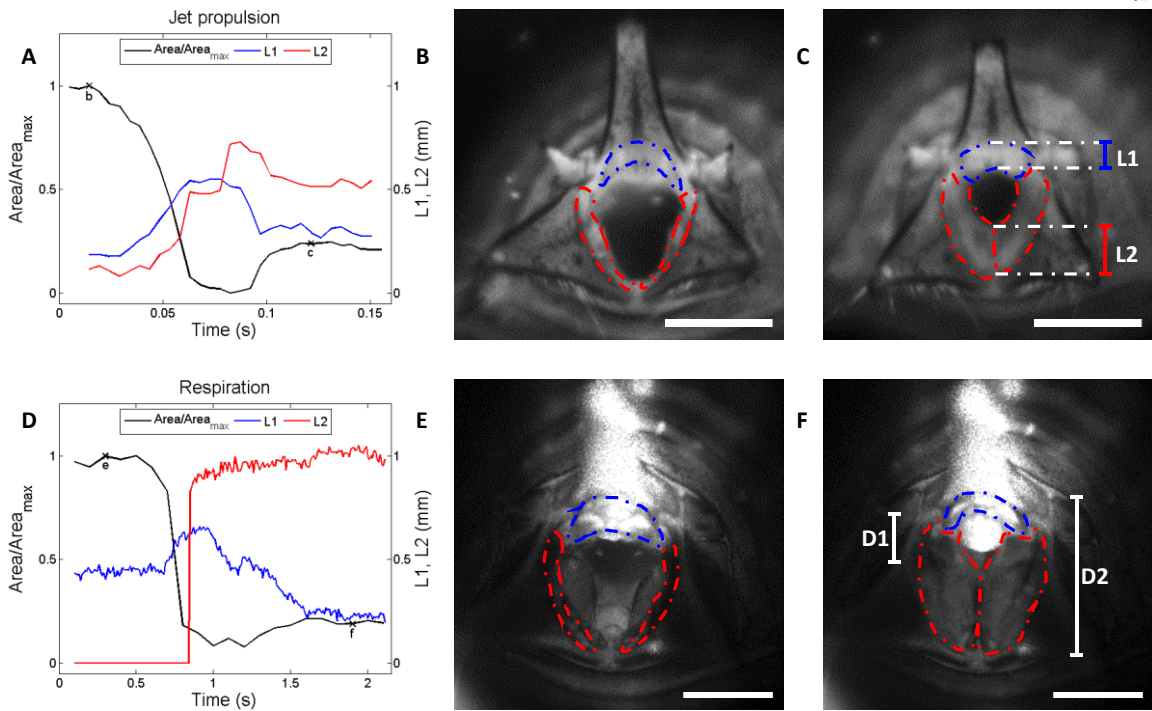


Figure 4.6 Asymmetry in anal valve kinematics. L1 = Distance between top and bottom of the top leaflet. L2 = Distance covered when the bottom two leaflets meet to cover the anal opening. D1 = diameter of the anal opening. D2 is the vertical length of the entire valve. (A) Time history curves of the anal opening area, L1 and L2 of jet propulsion transitioning from inhalation to exhalation. The time history curves of L1 and L2 both show a downward slope during transition. (B) A typical anal valve configuration during the refilling phase of jet propulsion. (C) A typical anal valve configuration during the jetting phase of jet propulsion. (D) Time history curves of anal opening area, L1 and L2 of respiration, transitioning from inhalation to exhalation. The time traces of opening area and L1 are similar to those of the jet propulsion mode. However, L2 curve does not slope down during the transition from inhalation to exhalation. (E) A typical anal valve configuration during the refilling phase of respiration. (F) A typical anal valve configuration during the jetting phase of respiration. Scale bar = 1 mm.

4.3.3 Degree of asymmetry and jet deflection angle

The degree of asymmetry (defined in section 4.2.1) and jet deflection angles are plotted together in figure 4.7. The jet deflection angle is measured with respect to the red reference line defined in figure 4.8B. The plot shows that the jet deflection angle increases as the degree of asymmetry increases. The flow direction of respiration ranged from -10.5°

to 33.1° ($n=6$; $\text{mean}=15.89^\circ$, $\text{s.d.}=5.96^\circ$). The flow direction of jet propulsion ranged from -5.3° to 3.3° ($n=3$; $\text{mean}=-0.73^\circ$, $\text{s.d.}=3.44^\circ$). The straight jet during jet propulsion is shown in figure 4.8A. The deflected respiratory jet is shown in figure 4.8B. Three additional cases of respiratory flow are shown in figure 4.9.

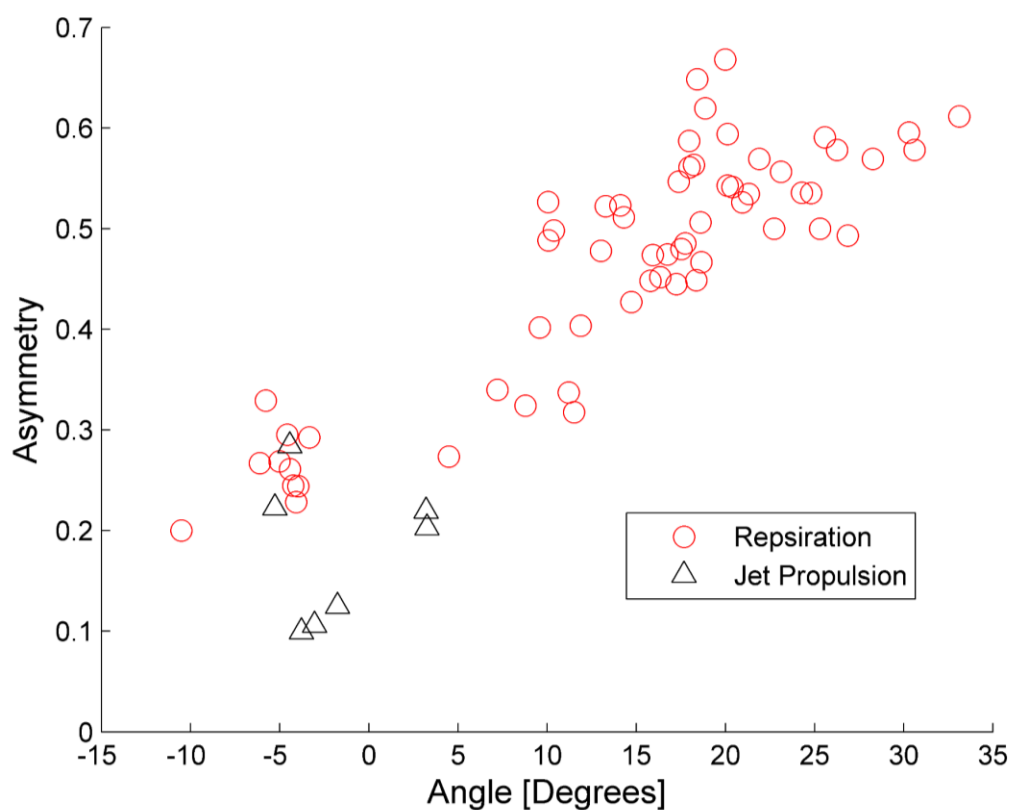


Figure 4.7 Relationship between the degree of asymmetry in anal opening and jet angle deflection. In all, 60 respiratory jets from 6 larvae, and 7 propulsion jets from 3 larvae were measured.

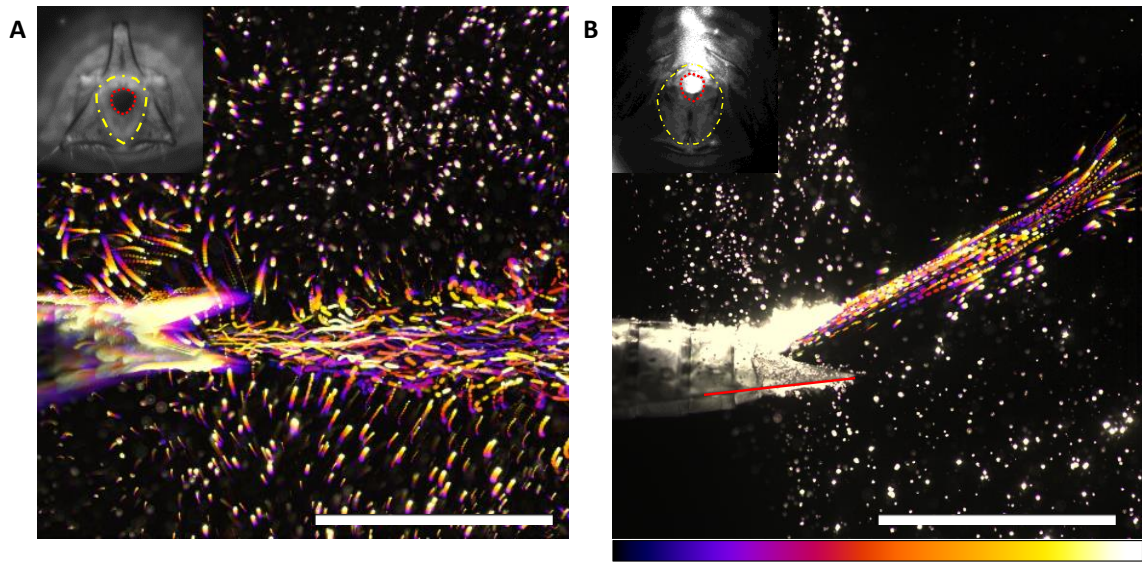


Figure 4.8 Directional variation of the jet. These images are pathline visualisations obtained by overlaying 13 images recorded at 250 frames per second. Color represents time, progressing from black to white (see color bar at the bottom of panel (B)). The top left corner of each panel shows a typical valve shape, where the complete valve is traced in yellow and the opening is traced in red. The valve configuration and flow were measured in separate experiments. Scale bar = 10 mm. (A) Exhalatory jet of the jet propulsion. The jet is straight with respect to the larva's abdomen. (B) Exhalatory jet of the respiration. The jet is deflected upward with respect to the larva's abdomen. The red line indicates the reference line from which the jet angle is measured.

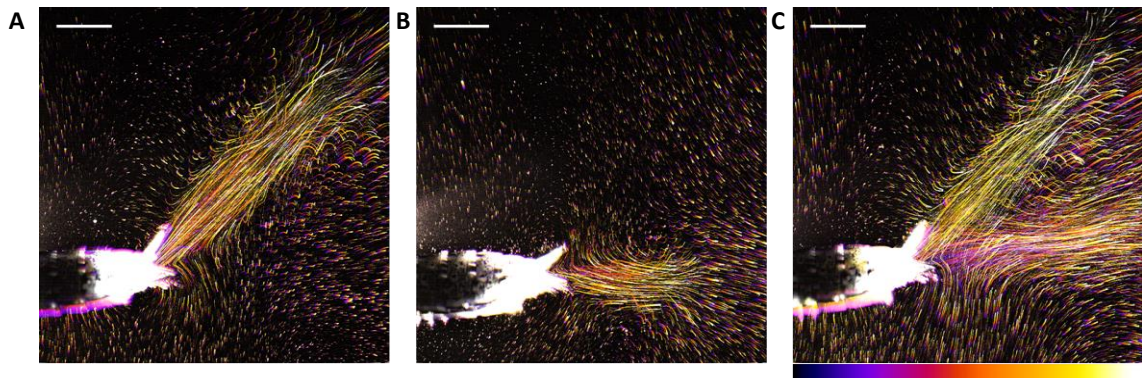


Figure 4.9 Directional variation within the respiratory jet. Scale bar = 5 mm. (A) A diagonally deflected respiratory jet. (B) Straight jet. (C) Diagonal and straight jets. The dragonfly larva switched the flow direction during a single exhalation phase. Color represents time, progressing from black to white (see color bar at the bottom of panel (C)).

4.3.4 Deflected respiratory flow: entrainment and refilling flow

The respiratory jetting and refilling flows are visualized in figure 4.10. Compared to figure 4.8B, more frames were overlaid to visualize the slower flow features, such as entrainment and refilling flow. An ensemble averaged velocity field of the entrainment flow and refilling flow are shown in figure 4.11B-D. The direction of the entrainment flow in the lower vicinity of the jet is orthogonal to the jet direction (Figure 4.10A, 11C). The refilling flow resembles sink flow; however, a stagnation point forms because of the flow reversal (Figure 4.9B). Both the pathline visualization and the velocity field show that the entrainment flow and the refilling sink-flow flow in a similar direction at the lower vicinity of the jet (Figure 4.10, 4.11C-D).

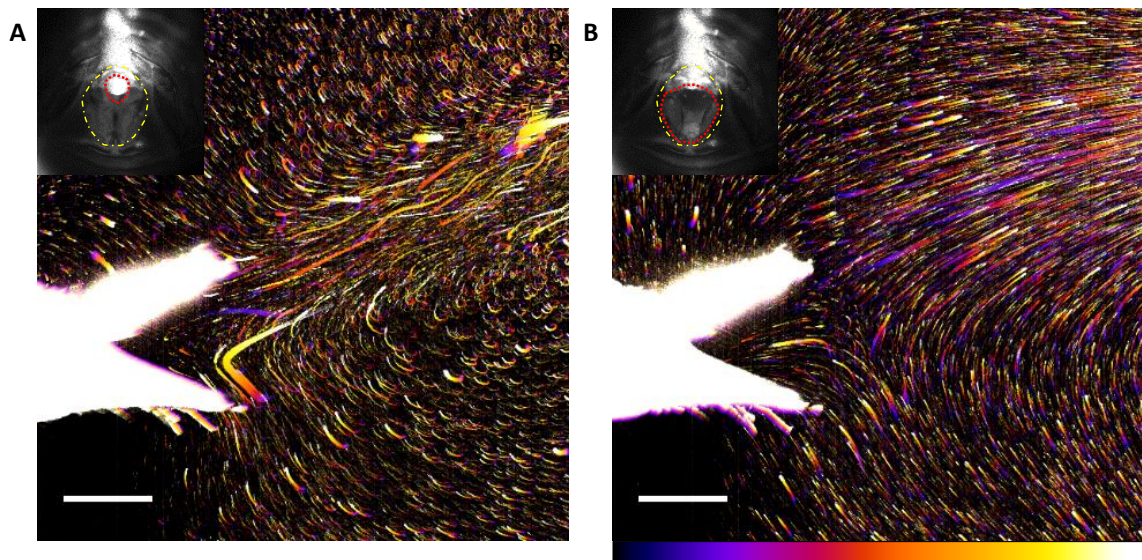


Figure 4.10 Details of the respiratory flow. Pathline visualisations similar to those in Figure 3, but with a longer integration by overlaying 256 images for (A) and 361 images for (B). Scale bar = 2 mm. (A) Near-field flow during the exhalation phase of respiration. This close up and longer time integration shows the slower entrainment flow direction. (B) The flow direction during the inhalation phase. The flow entering the valve originates from the lower periphery of the jet. The top left corners of (A) and (B) panels show typical valve shapes, where the complete valve is traced in yellow and the opening is traced in red. The valve configuration and flow were measured simultaneously.

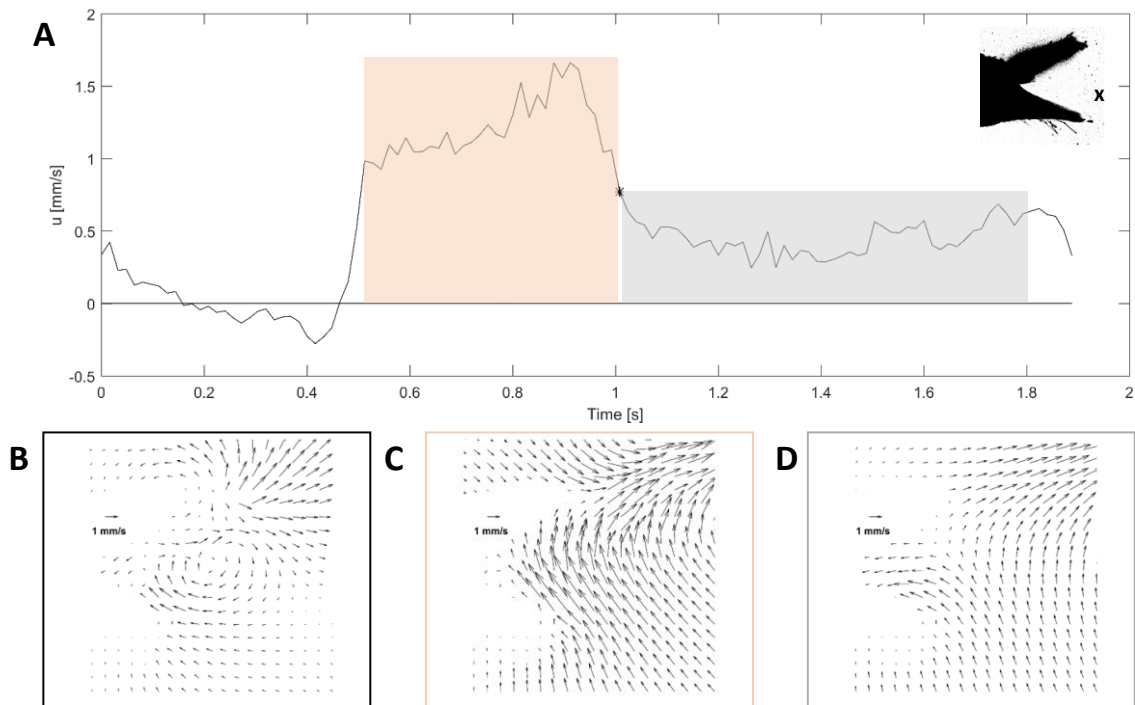


Figure 4.11 Quantitative analysis of the entrainment flow. (A) Time-history plot of a flow at single location. ‘*’ marks the transition. (B) Initial roll up of a vortex. (C) Entrainment flow field. Flow field corresponds to the orange box. (D) Refilling flow field. Flow field corresponds to the orange box

A temporal variation of the horizontal velocity at the jet’s lower vicinity marked with ‘x’ is plotted in figure 4.11A. The fluid at this location flow towards the jet exit, even during the jetting phase due to the deflected entrainment flow. In fact, the horizontal velocity of the entrainment flow is 2-3 times faster than that of the refilling flow. The entrainment flow speed decreases as the cycle transitions to the refilling phase. However, the flow speed is maintained at a magnitude comparable to the inhalation flow speed.

Note that the positive horizontal velocity in the beginning of the jetting phase is the result of the jet emerging from the anal orifice. There is a subsequent increase in the entrainment flow due to the jet shear-layer roll up (Figure 4.11B).

4.3.5 Timing of events

The measurements made in chapters 3 and 4 are aligned in time and plotted together for a holistic view of the dragonfly larvae's ventilatory events (Figures 4.12, 4.13). The respiration mode measurements are plotted in figure 4.12. The propulsion mode measurements are plotted in figure 4.13. The dotted vertical lines mark some of the important ventilatory events. The descriptions of each line are in the figure captions.

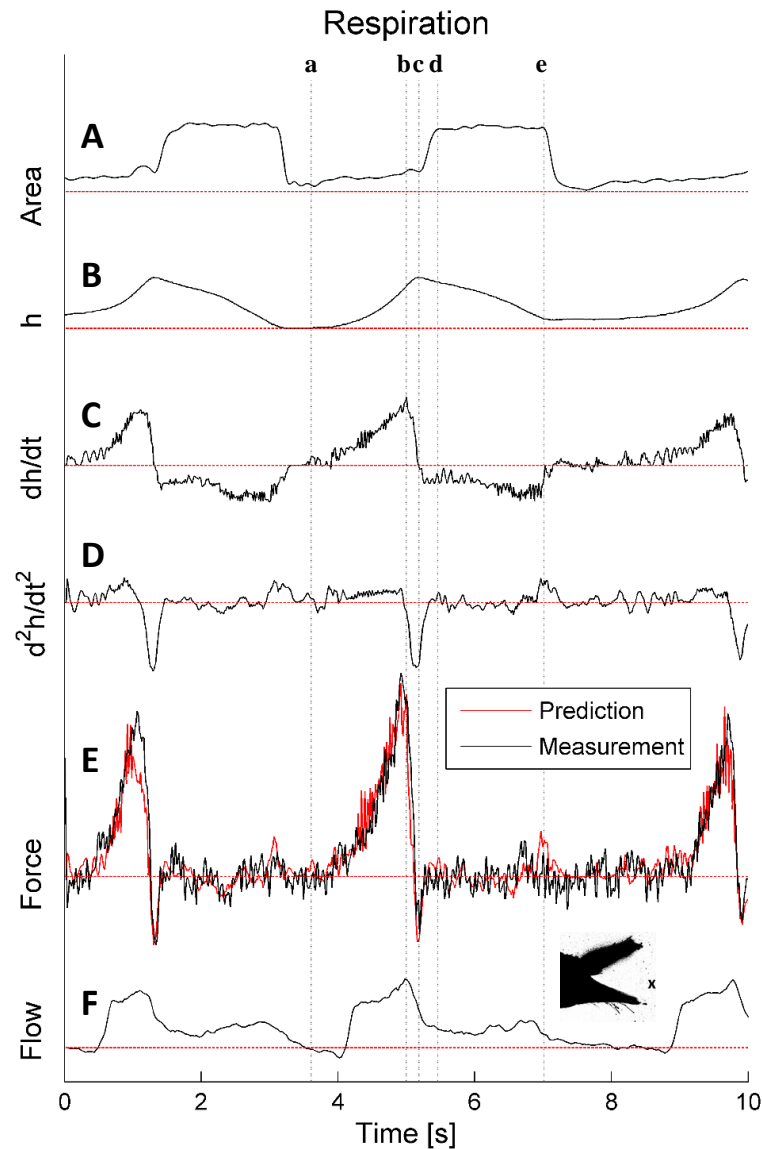


Figure 4.12 Respiratory anal valve and body kinematics and force measurement. (A) Variation in orifice opening area over time. (B) Height variation of the sixth sternum over time. Rise of the height signifies compression of the chamber. (C) First derivative of the height variation with respect to time. (D) Second derivative of height variation with respect to time. (E) Force measurement and force prediction based on equation 3.7. The normalisation of the predicted value is described in the results. (F) Time history plot of horizontal velocity component at the lower periphery of the jet (marked with x). Positive flow means flow directed towards left. Red horizontal lines indicate 0 points for each curve. Vertical dotted lines mark several key events. Line a marks the beginning of exhalation. Line b is when dh/dt is at the maximum. Line c marks the maximum sternum height, which indicates the end of exhalation phase. Line d indicates complete dilatation of the anal valve. Line e indicates the end of inhalation.

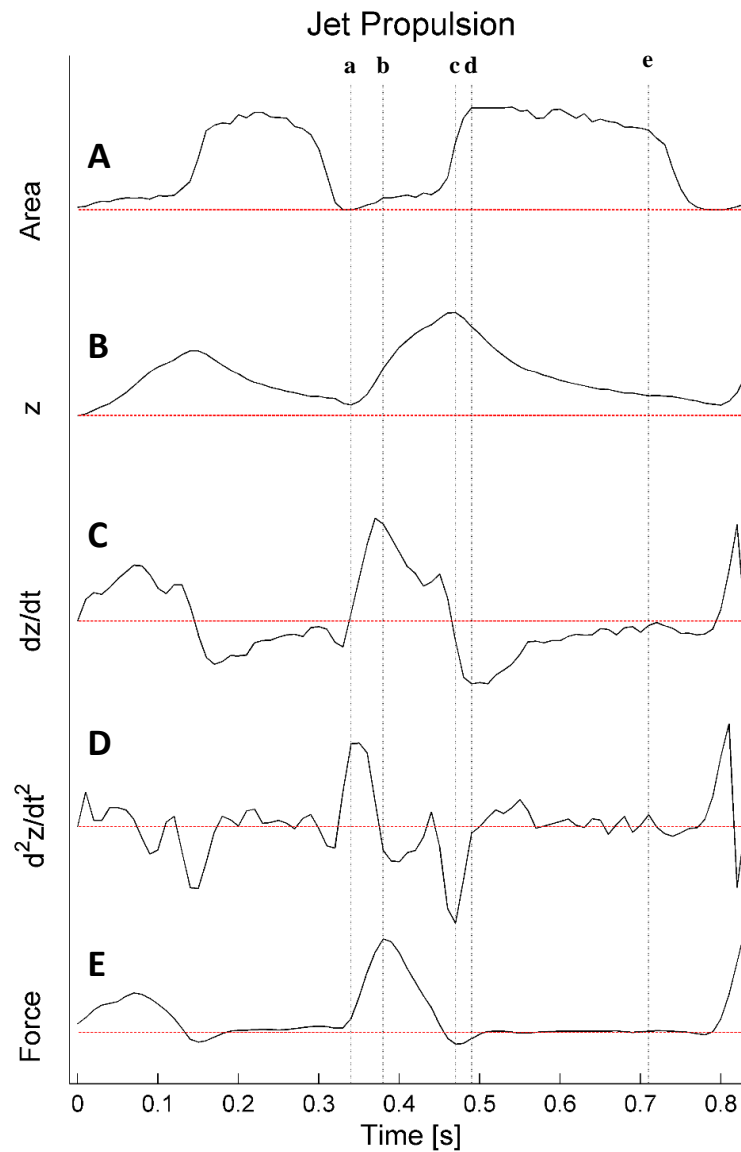


Figure 4.13 Jet propulsion anal valve and body kinematics and force measurement. (A) Variation in orifice opening area over time. (B) Length variation of the abdomen over time. Rise in the length signifies shortening of the length, and thus compression of the chamber. (C) The first derivative of the length variation with respect to time. (D) The second derivative of the length variation with respect to time. (E) Force measurement. Red horizontal lines indicate 0 points for each curve. Vertical dotted lines mark several key events. Line a marks the beginning of the jetting phase. Line b is when force is at the maximum. Line c marks maximum longitudinal contraction, which indicates the end of the jetting phase. Line d indicates complete dilatation of the anal valve. Line e indicates the end of the refilling phase.

4.4 Discussion

4.4.1 Aperture size effect on respiration

For the aquatic tidal respiration of larvae to be effective, re-inhalation of oxygen-depleted exhaled jet should be prevented, and energy usage should be efficient. In particular, reinhalation becomes a potential problem because these particular species of larvae live in a quiescent flow environment and remain immobile during respiration, which could deplete oxygen in the vicinity.

Mill and Pickard (1972) suggested that a small aperture during the respiratory jetting phase sends the jet far away to prevent reinhalation. Regardless of the opening asymmetry (Fig. 5F), argument for small aperture effect is compelling as follows. The mass conservation equation, $Q=uA$ (where Q is volumetric flux, u is jet velocity, and A is the orifice area) shows that a smaller orifice results in a faster flow given the same volumetric flow rate. In the respiratory jetting phase, the orifice opens to about one-fifth of the maximum opening, which would allow the flow speed to be five times faster than that obtained by the fully dilated valve jet. The high-velocity jet would send exhaled jet afar, leaving fresh water in the vicinity of the nozzle.

With this reasoning, further nozzle constriction would prevent reinhalation even better. However, the flux term in equation (3.3) shows that, as the orifice narrows, larvae have to provide more power to maintain the same volumetric flow rate. If the area is cut in half, they would have to provide four times more power to maintain the same flow rate. Moreover, for a small aperture, thrust is increased, which is counterproductive for larvae trying to remain immobile. These potential increases in inefficiencies may be the reason why further constriction of the valve opening is undesirable.

Moreover, the aperture dilatation during the inhalation phase also reduces the power required to refill the chamber. The power required for accelerating the sink flow varies inversely with the radius of the orifice (equation 3.3 half-sink term). Therefore, by dilating the orifice at the beginning of the suction, the larvae would reduce the power required to accelerate the fluid.

4.4.2 Aperture size effect on jet propulsion

The primary purpose of jet propulsion is to generate thrust. The small opening of the nozzle enhances the thrust. During the jetting phase, a quasi-steady thrust is given by equation (3.4), which shows that thrust is inversely proportional to the area of the nozzle opening. Thus, the small orifice of the larvae would increase the thrust. However, as mentioned in the previous section, it is important to note that decreasing the orifice area while maintaining volume flux requires more power. Since dragonfly larvae is limited in power, once the maximum power is reached, a further decrease in valve orifice will reduce the thrust as $T \propto P_{\text{max}}^{2/3} * A^{1/3}$. The limitation imposed by power might be the reason that further constriction of the aperture is undesirable.

The refilling phase aperture size does not influence the total impulse of the ventilatory cycle. This is because half-sink term has zero net contribution to total impulse (Figure 3.8B). However, smaller orifice does require more power to accelerate fluid (equation 3.3 half-sink term). Assuming available power during refilling is also limited, increasing the orifice size allows for a faster gain of high volume flux, which reduces time spent on refilling the chamber. As discussed in section 3.4.2, a decrease in refilling time increases the average

thrust. Therefore, one of the advantages of enlarging the refilling orifice could be the increased average thrust caused by the reduced refilling time.

4.4.3 Effect of independent movement of the leaflet in respiration

During respiration, not only do larvae constrict the valve, but they also place it asymmetrically by retracting only the top leaflet. The angle of the jet deflection increases with the increase in degree of asymmetry (Figure 4.7). The deflection of the respiratory jet is likely caused by the asymmetric valve opening. Here, two possible reasons are provided. First, a vertical pressure gradient might be generated by the pressure rise at the stagnation near the closed portion of the nozzle. This pressure gradient could push the fluid upward, deflecting the jet. The jet deflection through asymmetrically located opening is reported briefly in Appendix 1.

Second, the proximity of the nozzle opening to the top anal prong can result in the attachment of the jet to the oblique anal prong (Figure. 1A), which can further deflect the jet. The tendency of the jet to attach to a nearby solid surface is a well-studied phenomenon known as the Coandă effect (Wille and Fernholz, 1965). It was shown that the Coandă effect can deflect the jet in a similar Reynolds number range (Erath and Plesniak, 2006). In addition to these reasons, a three-dimensional contouring of the leaflets might influence the directionality of the jet.

In some cases, respiratory jets were not observed even though the laser was aligned with the body. This might signify that some of the jets were deflected sideways. The side-deflection might be attributed to the partial retraction of one of the bottom leaflets.

The jet deflected by the asymmetric opening also changes the direction of the near-field entrainment flow. This is because the entrainment flow direction is fixed orthogonally

with respect to the jet direction. Therefore, entrainment flow field at the jet's lower vicinity has a horizontal velocity component that points towards the orifice.

The jet deflection and modified entrainment flow have two potential benefits during the refilling phase. First, the deflected jet leaves the jet's lower vicinity with oxygen-rich water. Second, the flow field that is already flowing towards the jet nozzle would mean less power is required for suction. As shown in chapter 3, the larvae need to provide power to establish a sink-like refilling flow (equation 3.3, half-sink term). Having a flow field that is already like a sink-flow means that the larvae would spend less energy establishing sink flow. Moreover, these potential benefits occurring at the lower vicinity of the jet are coupled with retraction of the bottom two leaflets (Figure 4.12 line c-d). The timely widening of the anal valve would allow easier access to the oxygen-rich water flowing towards the opening.

4.4.4 Effect of concurrent movement of the leaflet in jet propulsion

At the start of the jetting phase, the larvae increase their anal valve size from complete closure to a smaller opening through concurrent movement of the leaflets. The symmetric valve opening results in a straight jet. Aligning the jet direction with the swimming direction minimizes the thrust loss due to unnecessary side thrust generation. Therefore, the concurrent movement of the leaflets might be beneficial for directing the thrust in the direction of escape.

PART 1 Concluding Remarks

In Part 1, the reciprocal jetting of dragonfly larvae was studied. This study made substantial progress in applying the Krieg and Mohseni (2015) model to live dragonfly larvae. Simple volumetric scaling and equation (3.7) worked very well in reproducing the force curves. Identifying dominant forces in each ventilatory phase gives more insight to why the dragonfly larvae might have a small anal opening during jetting phase and a large orifice during the refilling phase.

Progress was also made in discovering that the tri-leaflet anal valve is capable of deflecting the respiratory jet through independent control of the top leaflet. The entrainment flow directed towards the anal valve, and timely widening of the anal opening, suggested that the larvae might be using entrainment flow to partially refill the chamber. The contribution of the directed entrainment flow field in refilling the chamber would be interesting for future studies.

There are other types of ventilations such as gulping and chewing ventilations (Hughes and Mill, 1966; Tonner, 1936). A different valve kinematics is expected for these ventilatory events. Studying these ventilatory modes may expand the functionality of the dragonfly larvae's tri-leaflet valve. Other dragonfly families with different breathing patterns (e.g. Libellulidae) might also have different valve kinematics. Our findings may form a basis for understanding the mechanisms underlying these kinematics.

PART 1 References

- Alben, S., Miller, L. A. and Peng, J.** (2013). Efficient kinematics for jet-propelled swimming. *J. Fluid Mech.* **733**, 100-133.
- Anderson, E. J. and Grosenbaugh, M. A.** (2005). Jet flow in steadily swimming adult squid. *J. Exp. Biol.* **208**, 1125-1146.
- Anderson, E. J., Quinn, W. and De Mont, M. E.** (2001). Hydrodynamics of locomotion in the squid *Loligo pealei*. *J. Fluid Mech.* **436**, 249-266.
- Colin, S. P. and Costello, J. H.** (2002). Morphology, swimming performance and propulsive mode of six co-occurring hydromedusae. *J. Exp. Biol.* **205**, 427-437.
- Dabiri, J. O.** (2009). Optimal vortex formation as a unifying principle in biological propulsion. In *Annual Review of Fluid Mechanics*, vol. 41, pp. 17-33. Palo Alto: Annual Reviews.
- Dabiri, J. O., Colin, S., Katija, K. and Costello, J. H.** (2010). A wake-based correlate of swimming performance and foraging behavior in seven co-occurring jellyfish species. *J. Exp. Biol.* **213**, 1217-1225.
- Daniel, T. L.** (1983). Mechanics and energetics of medusan jet propulsion. *Can. J. Zool.* **61**, 1406-1420.
- Darwin, C.** (1964). *On the origin of species: A Facsimile of the First Edition with Introduction by Ernst Mayr.* Cambridge, Massachusetts USA: Harvard University Press.
- Erath, B. D. and Plesniak, M. W.** (2006). The occurrence of the Coanda effect in pulsatile flow through static models of the human vocal folds. *J. Acoust. Soc. Am.*

120, 1000-1011.

- Hughes, G. M.** (1958). The co-ordination of insect movements. 3. Swimming in *Dytiscus*, *Hydrophilus*, and a dragonfly nymph. *J. Exp. Biol.* **35**, 567-583.
- Hughes, G. M. and Mill, P. J.** (1966). Patterns of ventilation in dragonfly larvae. *J. Exp. Biol.* **44**, 317-333.
- Kohnert, S., Perry, S. F. and Schmitz, A.** (2004). Morphometric analysis of the larval branchial chamber in the dragonfly *Aeshna cyanea* Muller (Insecta, Odonata, Anisoptera). *J. Morphol.* **261**, 81-91.
- Krieg, M. and Mohseni, K.** (2013). Modelling circulation, impulse and kinetic energy of starting jets with non-zero radial velocity. *J. Fluid Mech.* **719**, 488-526.
- Krieg, M. and Mohseni, K.** (2015). Pressure and work analysis of unsteady, deformable, axisymmetric, jet producing cavity bodies. *J. Fluid Mech.* **769**, 337-368.
- Krieg, M., Sledge, I. and Mohseni, K.** (2015). Design considerations for an underwater soft-robot inspired from marine invertebrates. *Bioinspir. Biomim.* **10**, 065004.
- Krueger, P. S., Dabiri, J. O. and Gharib, M.** (2003). Vortex ring pinchoff in the presence of simultaneously initiated uniform background co-flow. *Phys. Fluids (1994-present)* **15**, L49-L52.
- Krueger, P. S., Dabiri, J. O. and Gharib, M.** (2006). The formation number of vortex rings formed in uniform background co-flow. *J. Fluid Mech.* **556**, 147-166.
- Krueger, P. S. and Gharib, M.** (2003). The significance of vortex ring formation to the impulse and thrust of a starting jet. *Phys. Fluids (1994-present)* **15**, 1271-1281.
- Krueger, P. S. and Gharib, M.** (2005). Thrust augmentation and vortex ring evolution in a fully-pulsed jet. *AIAA Stud. J.* **43**, 792-801.

- Mill, P. J.** (1972). Respiration in the Invertebrates. London: Macmillan Press.
- Mill, P. J. and Pickard, R. S.** (1972). Anal valve movement and normal ventilation in Aeshnid dragonfly larva. *J. Exp. Biol.* **56**, 537-543.
- Mill, P. J. and Pickard, R. S.** (1975). Jet-propulsion in Anisopteran dragonfly larvae. *J. Comp. Physiol.* **97**, 329-338.
- Pickard, R. and Mill, P.** (1972). Ventilatory muscle activity in intact preparations of aeshnid dragonfly larvae. *J. Exp. Biol.* **56**, 527-536.
- Pickard, R. S. and Mill, P. J.** (1974). Ventilatory movements of abdomen and branchial apparatus in dragonfly larvae (Odonata-Anisoptera). *J. Zool.* **174**, 23-40.
- Pickard, R. S. and Mill, P. J.** (1975). Ventilatory muscle activity in restrained and free-swimming dragonfly larvae (Odonata: Anisoptera). *J. Comp. Physiol.* **96**, 37-52.
- Rich, S. G.** (1918). The gill-chamber of dragonfly nymphs. *J. Morphol.* **31**, 317-349.
- Ruiz, L. A., Whittlesey, R. W. and Dabiri, J. O.** (2011). Vortex-enhanced propulsion. *J. Fluid Mech.* **668**, 5-32.
- Scott, G. G.** (1905). The distribution of tracheae in the nymph of plathemis Lydia. *Biological Bulletin* **9**, 341-354.
- Sledge, I., Krieg, M., Lipinski, D. and Mohseni, K.** (2015). Identifying and modeling motion primitives for the hydromedusae *Sarsia tubulosa* and *Aequorea victoria*. *Bioinspir. Biomim.* **10**, 066001.
- Snodgrass, R. E.** (1954). The dragonfly larva: Smithsonian Institution.
- Sutherland, K. R. and Madin, L. P.** (2010). Comparative jet wake structure and swimming performance of salps. *J. Exp. Biol.* **213**, 2967-2975.

Tonner, F. (1936). Mechanik und Koordination der Atem-und Schwimmbewegung bei

Libellenlarven. *Z. wiss. Zool.* **147**, 433-454.

Wille, R. and Fernholz, H. (1965). Report on the first European Mechanics Colloquium, on

the Coanda effect. *J. Fluid Mech.* **23**, 801-819.

Wu, D., Chen, M., Wang, Q., and Gao, W. (2013). Algae (Microcystis and Scenedesmus)

absorption spectra and its application on Chlorophyll a retrieval. *Front Earth Sci.* **7**, 522-530.

Part 2. Honeybee at the air-water interface: surfing with the capillary wave

PART 2 Introduction

Honeybees collect water for hive cooling, nectar dilution, and consumption (Lindauer, 1961). Water foragers often fall on the water surface (Moffett & Morton, 1973; Morton, Moffett & Martin, 1974), whereupon they are trapped by the water's adhesive force. Fortunately, they can float on the water surface with the buoyancy force provided by the large air sacs in their bodies (Snodgrass, 1910). Furthermore, the hair on the honeybee thorax prevents water from entering the thoracic spiracles, allowing the bees to breathe. However, unlike floating and breathing, escaping from the water surface requires a more dynamic intervention. Many honeybees are able to propel by vibrating their wings and often make it to shore.

The thrust generated by the bee is equal to the momentum transferred to the surrounding fluid. Therefore, measuring the momentum carried by the surrounding fluid can serve as a valuable tool in understanding the bee's propulsion. At the water surface, the fluid carry momentum both in the form of surface wave and flow.

CHAPTER 5: Honeybee at the air-water interface

5.1 Objectives

In this chapter, the honeybee's propulsion at the air-water interface is studied. The body motion and wing's interaction with the water surface is observed using high-speed videography. Based on the observation, a model describing the propulsion mechanism is suggested. The current study is limited to one particular orientation of the honeybee's fall, which results in a wetted ventral side and a dry dorsal side of the honeybee's wing and body.

5.2 Materials and Methods

5.2.1 Honeybee collection and experimental setup

Honeybees (*Apis mellifera*) were collected from a local garden on the Caltech campus in Pasadena, California, USA. They were dropped into a 27.5 cm (w) \times 21.3 cm (l) \times 5 cm (h) transparent water tank to simulate accidental falls into bodies of water (Figure 5.1). A series of measurements on tethered and untethered honeybees were performed. The depth of the water was maintained at 2.5–5 cm, which is much longer than the wavelength of the capillary-gravity wave generated by the honeybee. The temperature of the water was maintained at or above 18 °C.

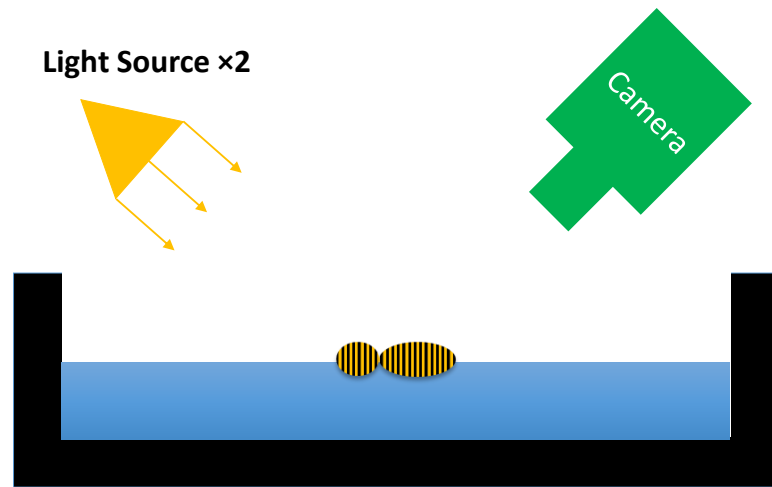


Figure 5.1 Schematic of experimental setup for high-speed videography.

5.2.2 High-speed videography of an untethered honeybee

Movies of freely moving bees were recorded at 800 frames per second using a high-speed camera (Dantec NanoSense Mk-III; Skovlunde, Denmark) facing the water surface at an angle of approximately 30 degrees with respect to the horizontal water surface (Figure 5.1). Two white light sources were placed on the sides of the water tank.

The honeybee's body motion was measured by analysing the movies in which the bees move straight across the image plane. x - t diagram of body motion is constructed via 'Reslice' function in ImageJ version 1.48 (National Institutes of Health, Bethesda, MD, USA). The slope of the line marked by the bee's body represent average speed. The slope was calculated by taking the cotangent of the angle measurement (Figure 5.2). The average propulsion speeds of 14 honeybees were measured along with their wing vibration frequencies.

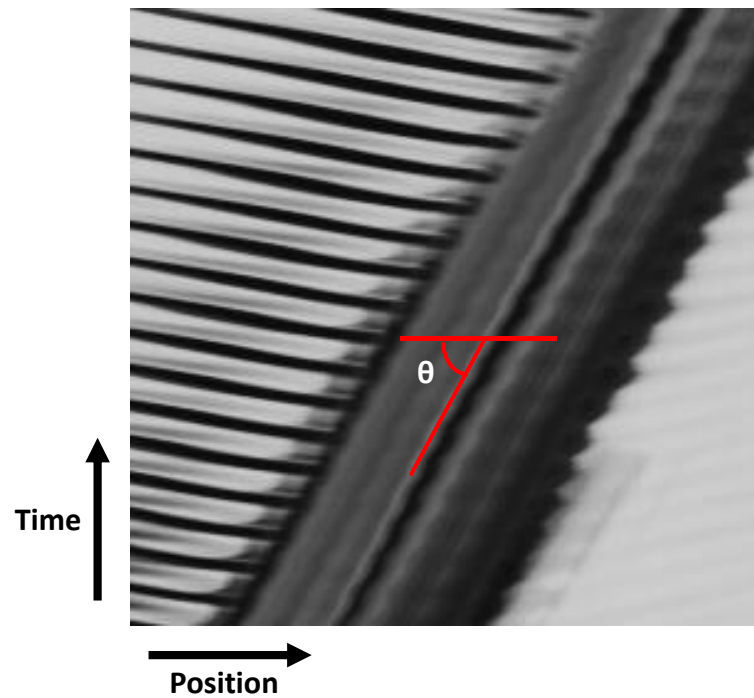


Figure 5.2 x-t diagram of the bee moving at the air-water interface. θ is used to find out the speed of the movement.

5.2.3 Body motion analysis

The body motion of one of the bees was analyzed in detail (60 Hz, 4 cm/s). The temporal variation of the body position was measured using the ‘StackProfile’ function in ImageJ. The resulting body position variation was discretely differentiated using the central difference method to find the instantaneous velocity and acceleration. The resulting velocity and acceleration curves were smoothed using the moving average function ‘smooth’ in Matlab 2016a (Mathworks, Natick, MA, USA) with a span of 5.

5.2.4 Tethering

A propelling bee only moves forwards. Therefore, constraining the forward motion was enough to keep the bee in one place. To do this, bees were guided into a bent metal wire fixed to a rigid structure (Figure 5.3). The width of the bent wire was adjusted so that it would sit in between the honeybee's head and thorax. A bee fixed in one place allowed a close-up view of the wing motion.

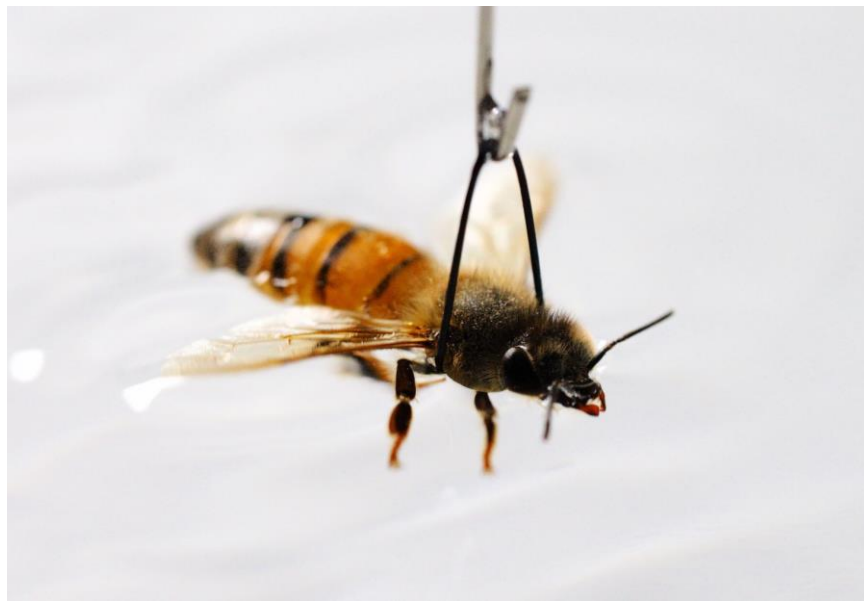


Figure 5.3 Tethered honeybee.

5.2.5 Wing kinematics and wing tip velocity

The wing kinematics of a tethered bee was recorded using a high-speed camera (Dantec NanoSense Mk-III; Skovlunde, Denmark) at 1000 frames per second. The wing tip velocity was measured by tracing the wing tip position. A total of three bees' wing tip velocity were measured.

5.3 Results

5.3.1 Wing frequency and propulsion speed

The wing vibration frequency ranges from 39 to 242 Hz. The average propulsion speed ranges from 1.9 to 4.3 cm/s. The two measurements of 14 bees are plotted together in figure 5.4. The horizontal error bar represents the standard error of 10 period measurements. The error bar is bigger for the higher frequency due to the measurement error, rather than the variation among periods. The variation in speed for each bees are not quantified, but figure 5.6 shows sinusoidal oscillation around the average velocity. Thus, similar oscillation with varying magnitude is expected for the other bees. The lower frequency generally had a larger amplitude of wing motion. Figure 5.5 shows amplitudes of 39 Hz, 59 Hz, and 242 Hz wing frequency.

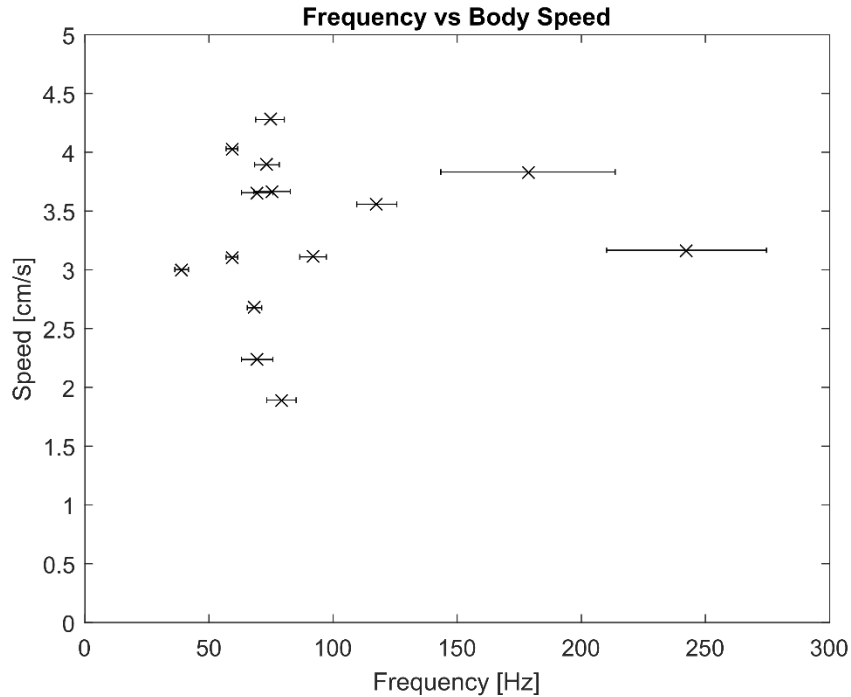


Figure 5.4 Wing vibration frequency versus average body speed. The error bar represent standard error of 10 measurements.

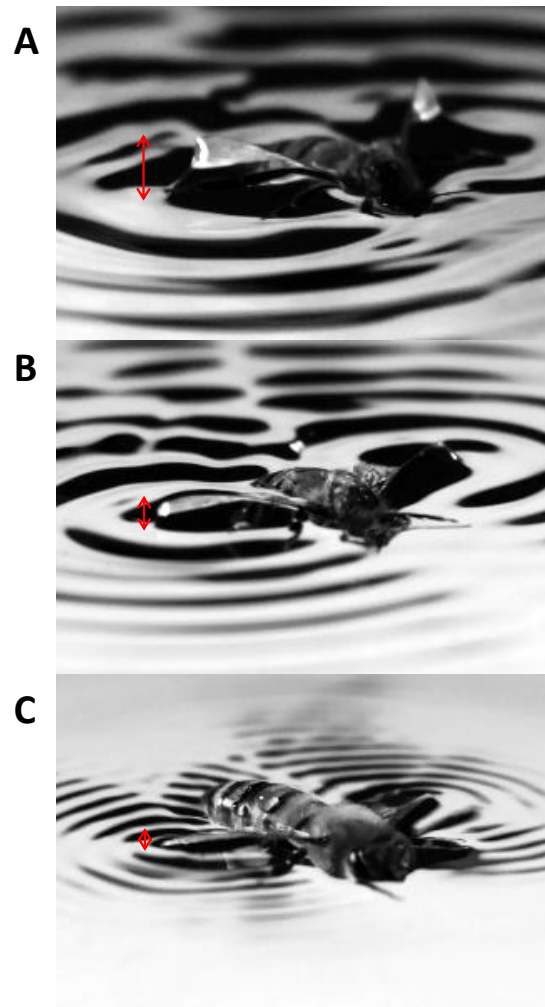


Figure 5.5 Amplitude of the honeybee's wing vibration.
(A) 39Hz. (B) 59Hz. (C) 242Hz.

5.3.2 Body motion

The velocity of honeybee's propulsion at the air-water interface oscillates, but maintains an average speed of approximately 3–4 cm/s (Figure 5.6). This speed corresponds to approximately three body-lengths per second. The frequency of the oscillation corresponds to the frequency of the wing motion. This confirms that the wing vibration is

responsible for the thrust. The acceleration curve is also oscillatory with a 90-degree phase shift from the velocity curve.

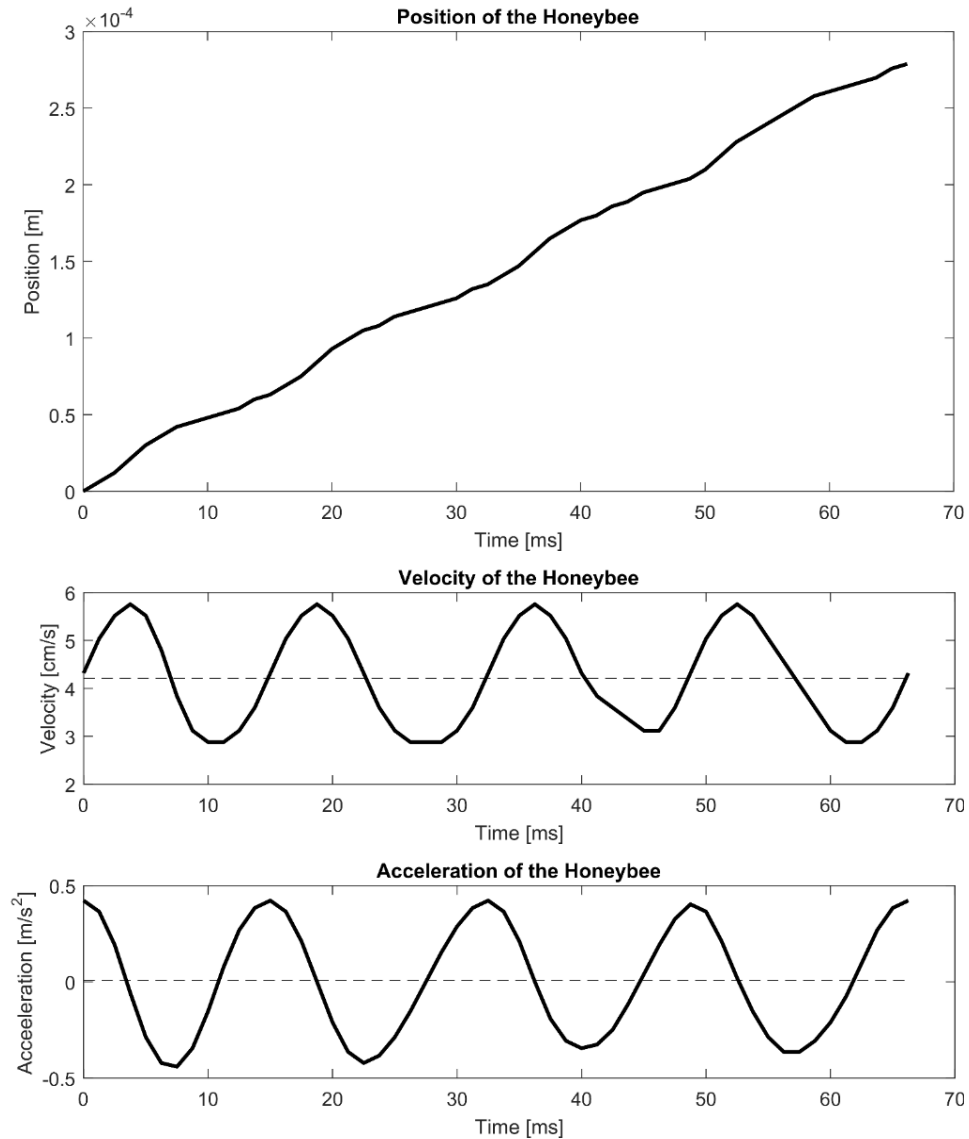


Figure 5.6 Honeybee's body position, velocity, and acceleration.
Wing vibration frequency = 59Hz.

5.3.3 Wing kinematics and interaction with water surface

The wing kinematics of the freely moving bee and the tethered bee are shown in Figure 5.7 and 5.8, respectively. A period of wing motion can be divided into stroke and

reversal phases. During the stroke phase, the wing supinates and rotates backwards relative to the bee's body (Figure 5.7A, 5.8A). As the wing moves backwards, a blob of water is pulled up at the ventral side of the wing. In the rear of the wing, a wave crest forms and travels backward.

During the reversal phase, the wing rotates forwards (Figures 5.7B, 5.8B). However, instead of pushing the water blob forwards at the supinated angle, the wing flattens and move over the blob. In the process, part of the water blob is pushed forward, but part of it continues to move backwards. A sketch of the cross-section of the wing interacting with the water surface is provided in figure 5.9D.

Comparing the wing motion with the body acceleration shows that the stroke phase and reversal phase correspond to the positive and negative acceleration, respectively (Figure 5.9B, C).

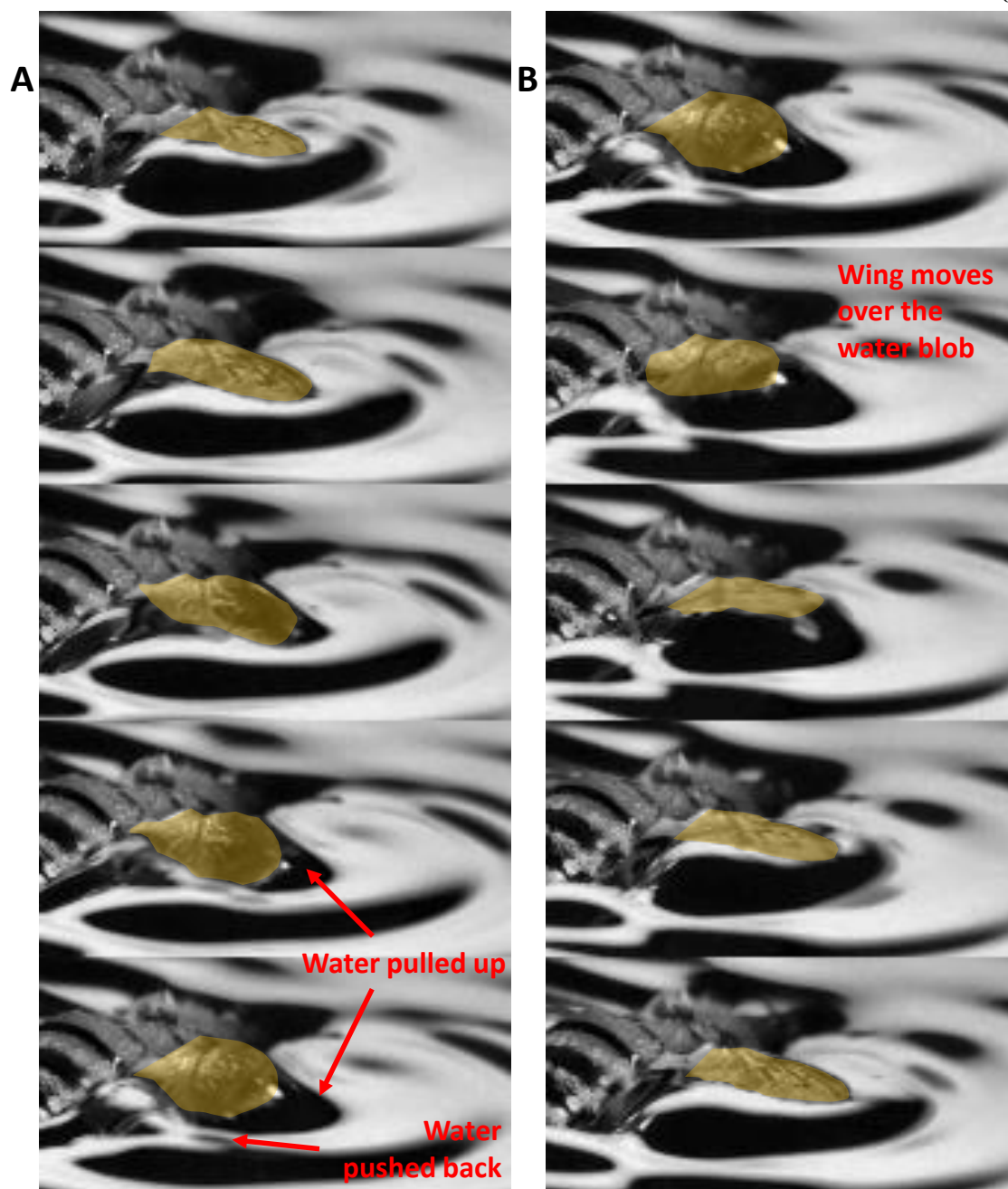


Figure 5.7. Wing kinematics of freely moving honeybee. The wing vibration frequency is 53 Hz. The wings are highlighted in yellow. (A) Stroke phase wing motion. (B) Reversal phase wing motion. The last image in (A) and first image in (B) are the same. Time interval between images is 2.5 ms.

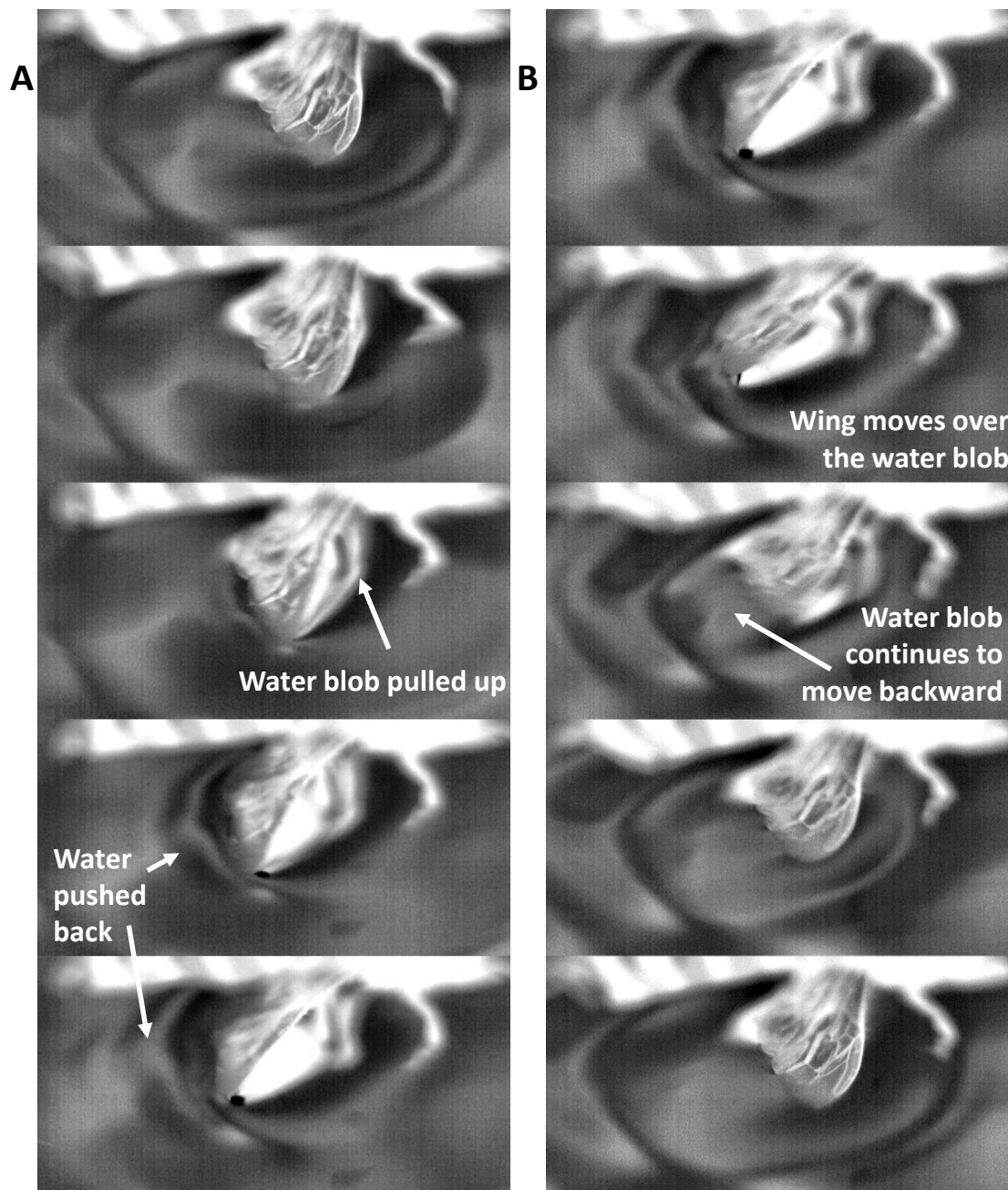


Figure 5.8 Wing kinematics of tethered honeybee. The wing vibration frequency is 47 Hz. (A) Stroke phase wing motion. (B) Reversal phase wing motion. The last image in (A) and first image in (B) are the same. Time interval between images is 3 ms.

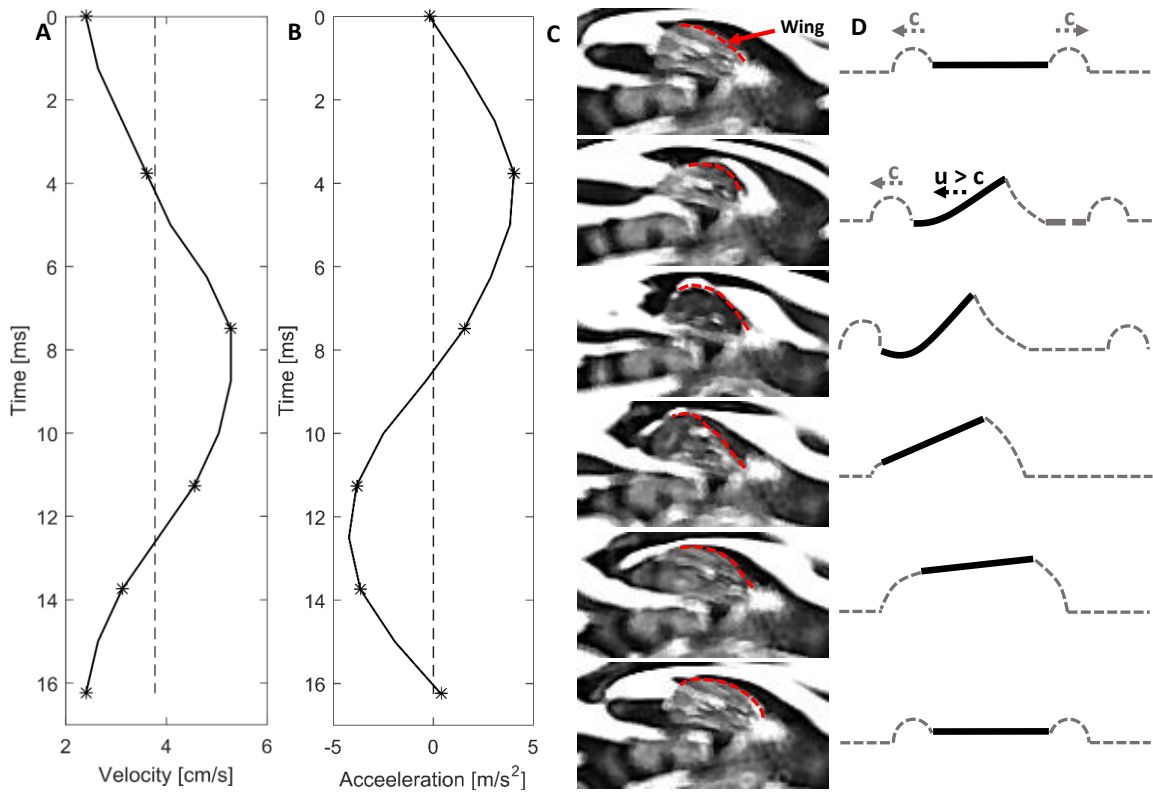


Figure 5.9 Body motion and corresponding wing motions. (A) Velocity of the bee's body. (B) Acceleration of the bee's body. The '*' corresponds to the wing kinematics sequence on the right. (C) Wing kinematics sequence. The leading edge of the wing is highlighted with red dashed lines. (D) Schematic of wing cross-section (black line) corresponding to C. Grey dashed line indicates the free surface. c is the characteristic speed of the surface wave formed at the end. u is the velocity of the wing. If $u > c$, wing would interact with the wave crest.

5.3.4 Wing tip velocity

The stroke phase wing tip velocity is measured for tethered honeybees with 40Hz, 47Hz and 67 Hz wing vibration frequency. The wing tip speeds were 31 cm/s, 41 cm/s, 32 cm/s. These speeds all exceed minimum phase velocity of the capillary-gravity wave ($c_{\min} \sim 23 \text{ cm/s}$ at 25°C).

5.4 Discussion

5.4.1 Frequency and speed range

Most of the honeybee's wing beat frequency at the water surface is substantially lower than the wing frequency of 200–250 Hz during flight (Altshuler et al., 2005). In the case where wing frequency is close to that in flight, the amplitude of the wing motion is significantly reduced. One possible reason for the reduced amplitude is due to the attached water effectively increases the inertia of the wing, thereby requiring much more power if it were to vibrate at the same amplitude. Another possibility for the varying amplitude is the varying hydrophobicity of the wing. A more hydrophilic wing may anchor the wing more firmly to the water surface, while a more hydrophobic wing may experience much reduced adhesion. What is surprising is how the high frequency vibration and low frequency vibration achieve similar propulsion velocity. However, more data points are needed to validate this trend.

5.4.2 Wave drag

When an object on the free surface moves at a speed exceeding the minimum capillary-gravity wave speed, a pressure disturbance accumulates in front of the object, much like a shock wave. The accumulated pressure pushes the water surface, forming wave crests. Several studies have shown that the object generating these wave crests

experiences extra drag, known as wave drag (Burghlea and Steinberg, 2002). The honeybee's stroke phase wing speed exceeds the minimum capillary-gravity wave speed. Therefore, the backward rotating wing would experience resistance in the form of wave drag.

Another possible source of resistance is the uneven surface at the onset of the stroke phase. At the end of the reversal phase, part of the water blob pulled up continues to move backwards. The raised interface at the rear of the wing provides a surface on which the wing's trailing edge can push against. This, too, requires the wing to move faster than c_{\min} , because the uneven surface itself is a wave. A wing moving slower than c_{\min} will not reach the wave.

The wave crest observed at the rear of the rotating wing (most clearly visible in figure 5.8A) can be a newly formed wave crest by the fast rotating wing, or an existing surface wave whose magnitude is intensified by the fast rotating wing (Figure 5.7A, 5.8A).

5.4.3 Model

Here, a model describing how the wing motion generates thrust is proposed. During the stroke phase, the fast rotating wing generates a wave at its trailing edge, while pulling up a blob of water with its ventral side. Pushing on the wave crest and pulling up the blob of water add resistance to the moving wing. Any force resisting wing motion generates an equal and opposite force on the bee's body, in accordance with Newton's third law. In other words, the resistance from the attached water blob and the rear wave temporarily anchor the rotating wing, thereby pushing the bee's body forwards

(illustrated in Figure 5.10) . The positive acceleration of the propelling bee corresponds to the stroke phase, which is consistent with the proposed model (Figure 5.9B, C).

During the reversal phase, the wing moves over the water blob attached at its ventral side. Such kinematics would reduce the wing's interaction with the water blob, decreasing the resistance. This can be viewed as releasing the attached water mass. Thus, during the reversal phase, the lightened wing would rotate forwards, rather than the body moving backwards (illustrated in Figure 5.10). Without the reduced interaction, the bee's body would be pushed back close to its original position. Although the bee's body do decelerates during the reversal phase (Figure 5.9), the full period of wing motion maintains an average velocity of approximately 4 cm/s. The deceleration is likely due to both the drag on the body and diminished but remaining effect of reverse wing motion.

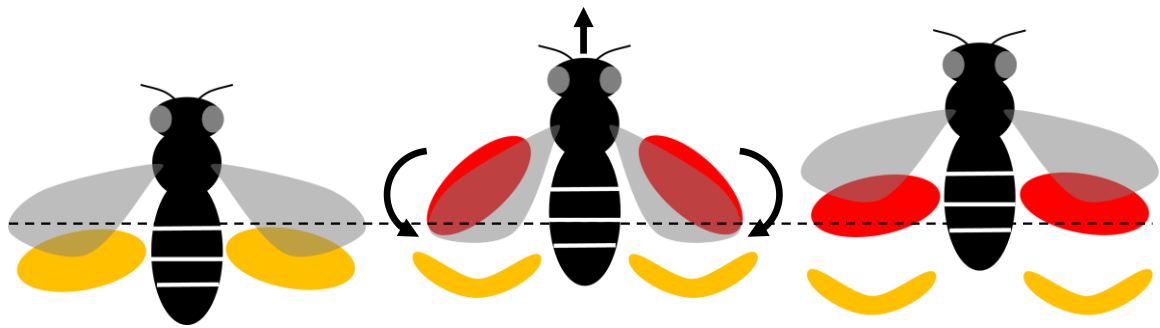


Figure 5.10 Illustration of the bee's propulsion mechanism. The yellow structures represent the water blob pulled up from the previous cycle. The red structure represent the newly pulled up water blob. During the stroke phase, the newly pulled water blob and rear wave crest anchor the rotating wing and push the bee's body forwards. During the reversal phase, the wing moves over the water blob. The lightened wings rotate forward instead of the bee's body.

Note that the water blob under the wing that has been pulled to reach the speed exceeding c_m is like a capillary wave crest. Thus, the wing constantly generates capillary waves and moves over them, all the while neither penetrating nor detaching from the water surface. This interaction between the wing and the water surface resembles surfing on the self-generated capillary wave. The difference with traditional surfing would be that instead of the wave pushing on a surfer, a surfer is pulling on the wave. Another difference is that while traditional surfing uses gravity wave, the bee's surfing uses capillary wave.

5.4.4 Why not jump out of the water?

Organisms at the water surface, whether they are on it voluntarily or not, can escape by either jumping out or swimming to shore. Honeybees have a large wetted area (wings and abdomen) that are only moderately hydrophobic and their legs cannot impart large momentum downward, which render escape by jumping unlikely.

Jumping out of the water usually require a special adaptation. Water striders have superhydrophobic legs that keep the adhesive force of water to minimum (Lee and Kim, 2009). In addition, they adjust leg rotation speed in a way that exploits the elasticity of the free surface (Yang et al., 2016). Pygmy mole crickets are able to jump out of the water using their powerful hind legs with special spurs that spread out (Burrows and Sutton, 2012). The increased surface area allows them to impart large vertical momentum on the surrounding water, thereby thrusting themselves out of the water.

5.4.5 Comparison with other semi-aquatic insects' locomotion

Most water surface dwelling arthropods generate horizontal thrust by impacting the water surface with their legs (Hu and Bush, 2010) or by flapping their wings in the air

(Mukundaraian et al., 2016). A notable exception is Plecoptera, which uses its forewings for rowing (Marden and Thomas, 2003). Their rowing mechanism has a much lower wing frequency (17Hz) and the wing completely detach from the water, which distinguishes Plecoptera's rowing from the honeybee's propulsion. The described surfing-like propulsion mechanism is probably not limit to the honeybees, but may be used by other aerial insects that fall on the water. For example, the author has observed a larger carpenter bee propelling in a similar way.

CHAPTER 6: Flow and wave field

6.1 Objectives

In this chapter, the flow and wave patterns generated by the honeybee are visualized and measured. The average force imparted on the fluid is estimated through analysing the flow and wave field. The average thrust was also calculated from the honeybee's body motion. The order of magnitude of the two results are compared.

6.2 Materials and Methods

6.2.1 Average thrust and body motion

The force balance on the honeybee's body (Figure 6.1) is given by

$$M(1 + \alpha) \frac{dU}{dt} = C_D A \rho \frac{U^2}{2} + F_{wing}(t) \quad (6.1)$$

where M is the mass of the bee, α is the added mass coefficient, U is the velocity of the body, C_D is the coefficient of drag, A is the frontal area, ρ is the density of water, F_{wing} is the force generated by the wing, and t is time.

Assuming dU/dt is a sine function with period equalling one wing motion, the time average of equation 6.1 becomes

$$\frac{C_D A \rho}{2T} \int_0^T (U(t))^2 dt = -\frac{1}{T} \int_0^T F_{wing}(t) dt \quad (6.2a)$$

$$\frac{C_D A \rho}{2} \overline{U^2} = -\overline{F_{wing}} \quad (6.2b)$$

where T is one period of wing motion and bar indicates time average. Therefore, the average force from a period of wing motion can be calculated from the velocity of the honeybee's body (Section 5.3.2, Figure 5.6).

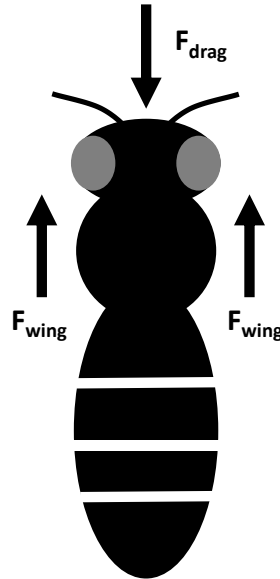


Figure 6.1 Horizontal force balance on bee's body.

F_{wing} =Force generated by the wing.

F_{drag} =form drag on the half-submerged bee.

6.2.2 Flow visualization

20- μm hollow glass particles (Potters Inc., Malvern, PA, USA) were used to visualize the flow generated by a tethered bee (see section 5.2.4 for tethering method). To visualize the surface streaming flow, buoyant glass particles were used. This was to ensure that the particles remained at the surface of the water. Buoyant particles were selected by mixing the particles with deionized water and collecting the particles floating on the surface. Light-emitting diodes (Neewer CN-160; Shenzhen, China) were used to illuminate the particles. The flow pattern was recorded with a high-speed camera (IMPERX 210P; Boca Raton, FL,

USA) at 100 frames per second. A schematic of the experimental setup is provided in figure 6.2A.

To visualize deeper water flow, neutrally buoyant particles were used. The neutrally buoyant particles were selected by mixing particles with deionized water and collecting the suspended particles after 4 hours. The flow 2.0 mm below the free surface was illuminated using a laser sheet. Images were recorded with a high-speed camera (Dantec NanoSense Mk-III; Skovlunde, Denmark) at 800 frames per second. The bee's wing vibration frequency was 65 Hz. The flow at the center plane (sagittal plane of the bee) behind the bee was also illuminated using a laser sheet. Images were recorded with a high-speed camera (IDT-OS3-S3) at 1000 frames per second. The bee's wing vibration frequency was 58 Hz. A schematic of the experimental setup is provided in figure 6.2B.

The resulting sequences of particle images were used for pathline visualization and velocity field measurement. The pathlines were visualized by overlaying image sequences using the 'Z Project' function in ImageJ.

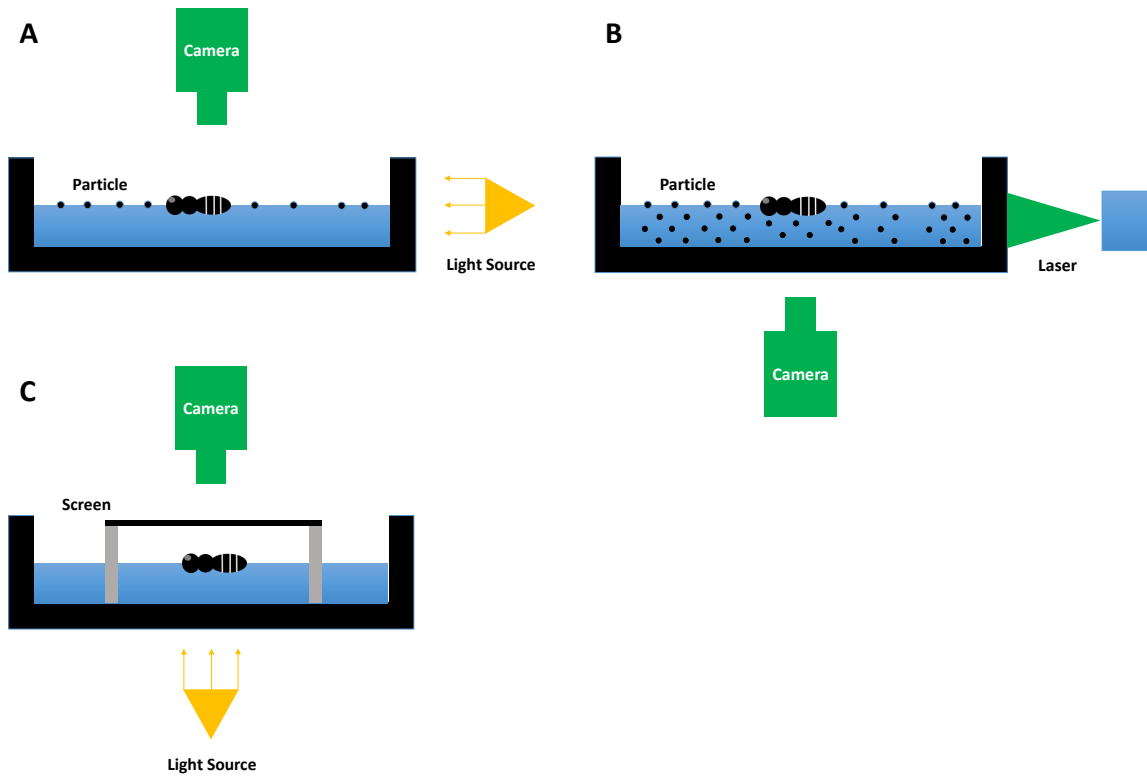


Figure 6.2 Schematics of three experimental setups. (A) Experimental setup for visualizing free-surface flow. (B) Experimental setup for visualizing deeper water flow. (C) Experimental setup for shadowgraph.

6.2.3 Particle Image velocimetry parameters

The velocity field was obtained using PIVview3C version 3.5.9 (PIVtech, Göttingen, Germany) with the following parameters:

- (1) 2 mm below the free surface: image pair offset, 8; 48×48 pixel windows size; 12 pixel overlap; standard Fast Fourier Transform correlation; multi-grid interrogation with 3 passes; maximum displacement limit, 5 pixel. Ensemble averaged over 4 second, equivalent of approximately 260 periods.
- (2) Center Plane: image pair offset, 10; 64×64 pixel windows size; 16 pixel overlap; standard Fast Fourier Transform correlation; multi-pass interrogation; maximum

displacement limit, 10 pixel. Ensemble averaged over 1.5 second, equivalent of approximately 87 periods.

6.2.4 Shadowgraph

A schematic of the experimental setup is provided in figure 6.2C. A parallel white light source was generated by placing a point light source at the focal point of a biconvex lens. The light rays travelled through the water and were projected on a light diffuser film, placed 1 cm above the water surface. A high-speed camera (Dantec NanoSense Mk-III; Skovlunde, Denmark) was set up opposite to the diffuser. The wave pattern produced by the untethered bee was recorded at 500 frames per second.

6.2.5 Momentum flux

A control volume around the bee is considered (Figure 6.6A, C). The momentum flux out of the control surface, C_s , through the fluid flow is approximated as

$$P_{flow} = \rho u^2 A \quad (6.3a)$$

where, P_{flow} is momentum carried by the flow, ρ is the density, u is the average velocity, and A is the area. Here, u and A are assumed to be constant; thus, the expression is equivalent to average force,

$$\overline{F_{flow}} = \rho u^2 A \quad (6.3b)$$

where $\overline{F_{flow}}$ is average force applied to surrounding fluid in generating flow.

The momentum carried by one wavelength of surface wave can be obtained through considering radiation stress, S_{xx} , which is defined as “the excess flow of momentum due to the presence of a wave” by (Higgins and Stewart, 1964). For a capillary wave in deep water (depth \gg wavelength), the expression for radiation stress is given by

$$S_{xx} = \frac{3}{4} \sigma a^2 k^2 \quad (6.4)$$

where k is the wave number, a is the amplitude of the wave, and σ is the surface tension. The expression is derived for a 2-D case, therefore its unit is force per unit width. Multiplying by the width of the wave, W , the average force applied to surrounding fluid in generating one wavelength of surface wave, $\overline{F_{wave}}$, can be expressed as

$$\overline{F_{wave}} = S_{xx} \times W = \frac{3}{4} \sigma a^2 k^2 W \quad (6.5)$$

The amplitude is measured from the raw center plane image (Figure 6.6D). The estimates of k and W will be given in section 6.3.4.

6.3 Results

6.3.1 Wave pattern

The shadowgraph images shows the wave pattern generated by the 70Hz vibrating wings (Figure 6.3A). The white and dark fringes are wave crests and troughs, respectively. The wave field shows bilateral symmetry, but lacks fore–aft symmetry (Figure 6.3A). An interference pattern forms at the rear of the bee, while the water surface in front lacks a strong wave. Figure 6.3B shows the shadowgraph sequence of one full period.

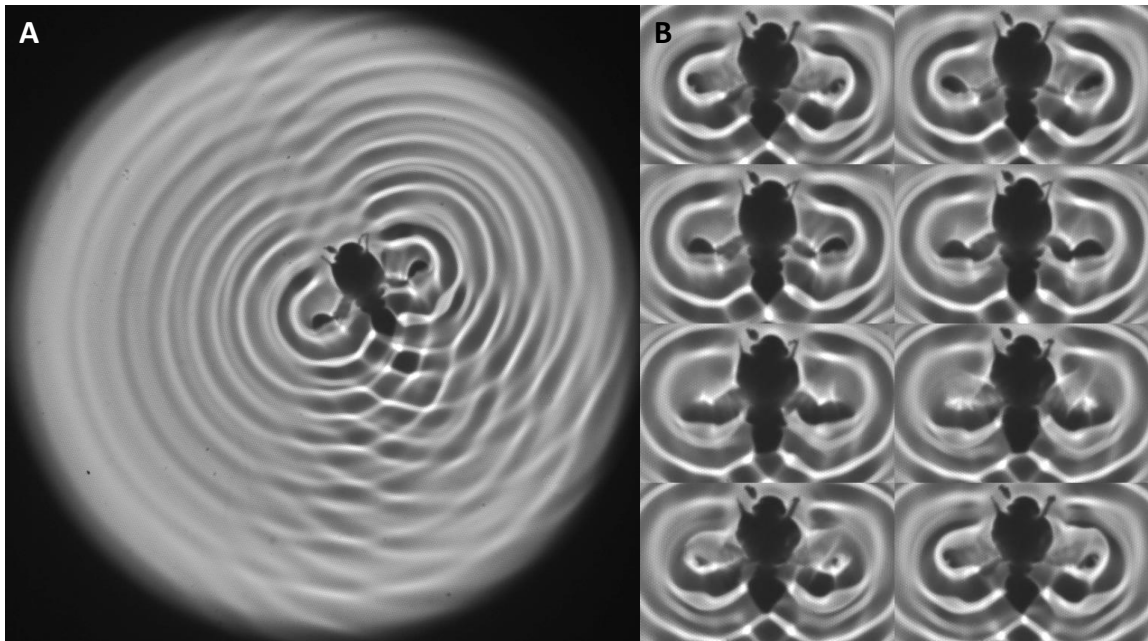


Figure 6.3 Wave pattern visualized using shadowgraph. Light and dark fringes indicate the wave crests and troughs, respectively. (A) Wave field. (B) Close-up of the shadowgraph images. Time interval between images are 2 ms. The sequence start from the image at the top left corner and zig-zags down.

6.3.2 Flow pattern

The vibrating wing generates a complex surface streaming flow (Figure 6.4A). The surface streaming flow can be characterized by three outward jets, three inward jets, and circulation regions between the jets (Figure 6.4C). However, of the three outward jets, only the backward flowing central jet is present 2 mm below the free surface (Figure 6.4B). The velocity field of the deeper water is shown in figure 6.5A. The center plane velocity field is shown in figure 6.5D. The max flow speed is approximately ~ 3 cm/s and the width and depth of the jet is approximately 1 cm x 1 cm.

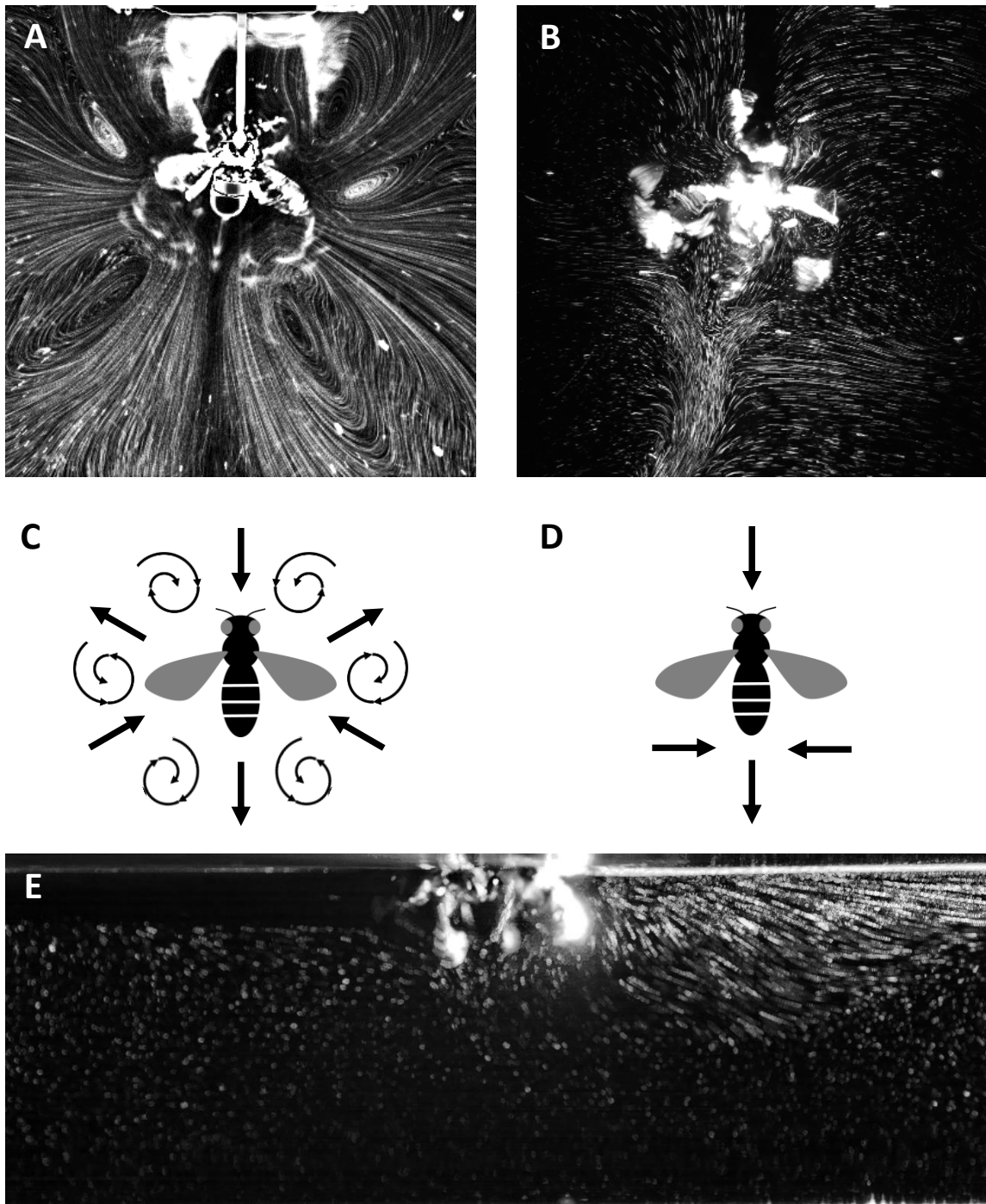


Figure 6.4 Flow generated by a tethered bee. (A) Surface streaming flow pattern (B) Deeper water flow 2.0 mm below the free surface. The tethered bees in A and B are slightly tilted. (C) Schematic of surface streaming flow. (D) Schematic of deeper water flow. (E) Center plane flow pattern.

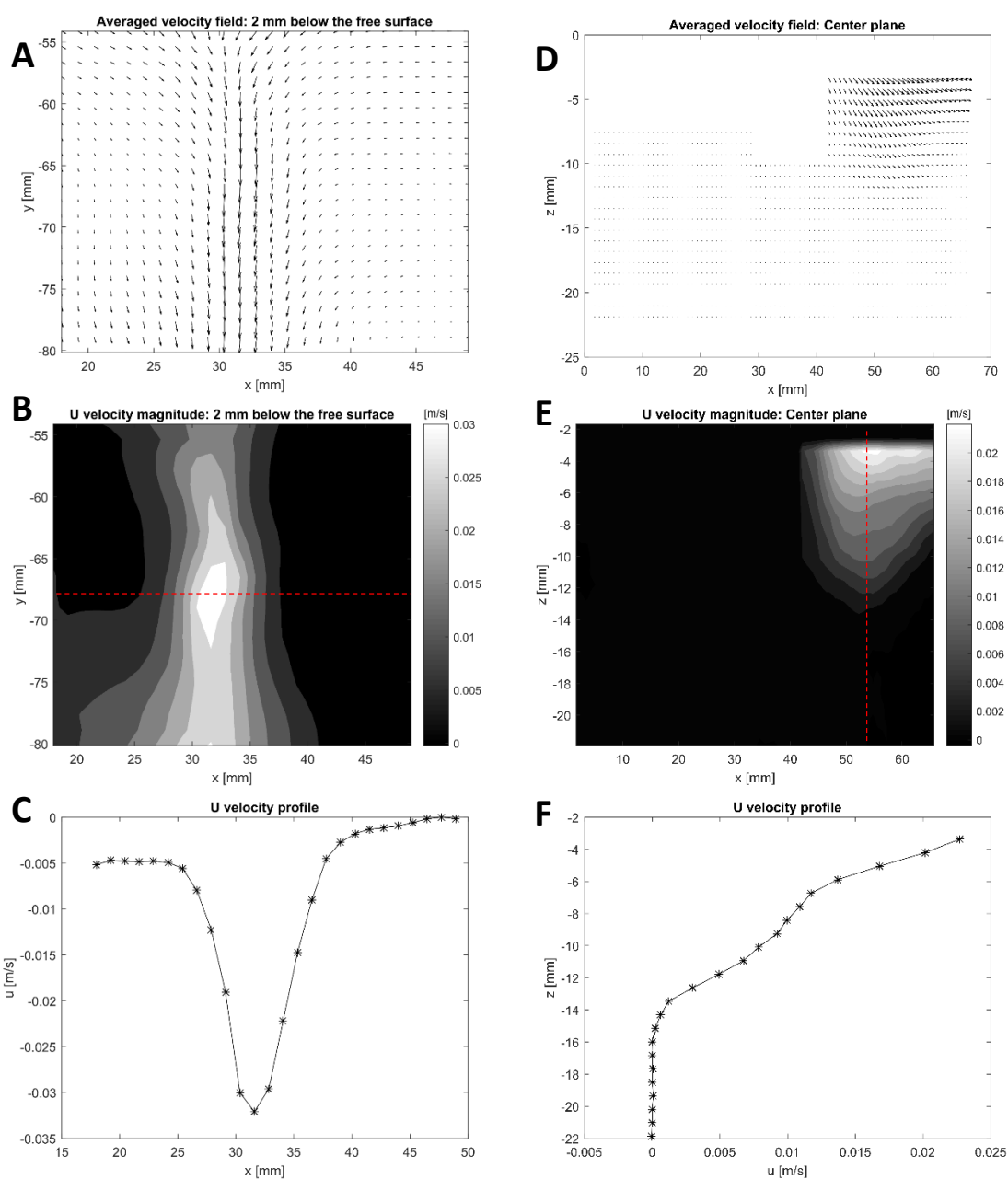


Figure 6.5 Flow velocity measurements. (A-C) Velocity measured at 2 mm below the surface. (A) Velocity field. (B) Contour plot of magnitude of U. (C) Profile of U at the red line on the contour plot. (D-F) Velocity measured at the center plane. (A) Velocity field. (B) Contour plot of magnitude of U. (C) Profile of U at the red line on the contour plot.

6.3.3 Average force calculation from the body motion

Here, equation (6.2b) is used to calculate average thrust generated by the honeybee. Assuming $C_D \sim 0.6-0.8$ (C_D of a sphere at $Re \sim 230-470$; Abraham, 1970), $A \sim 2.64 \times 10^{-5} \text{ m}^2$ (Based on the width of the dimple (hemisphere) made by the thorax $\sim 8.2 \text{ mm}$; Figure 6.6B), $\rho \sim 10^{-3} \text{ kg/m}^3$, and using the body speed data given in figure 5.6, the average force generated in one period of wing motion is approximately 30-40 μN .

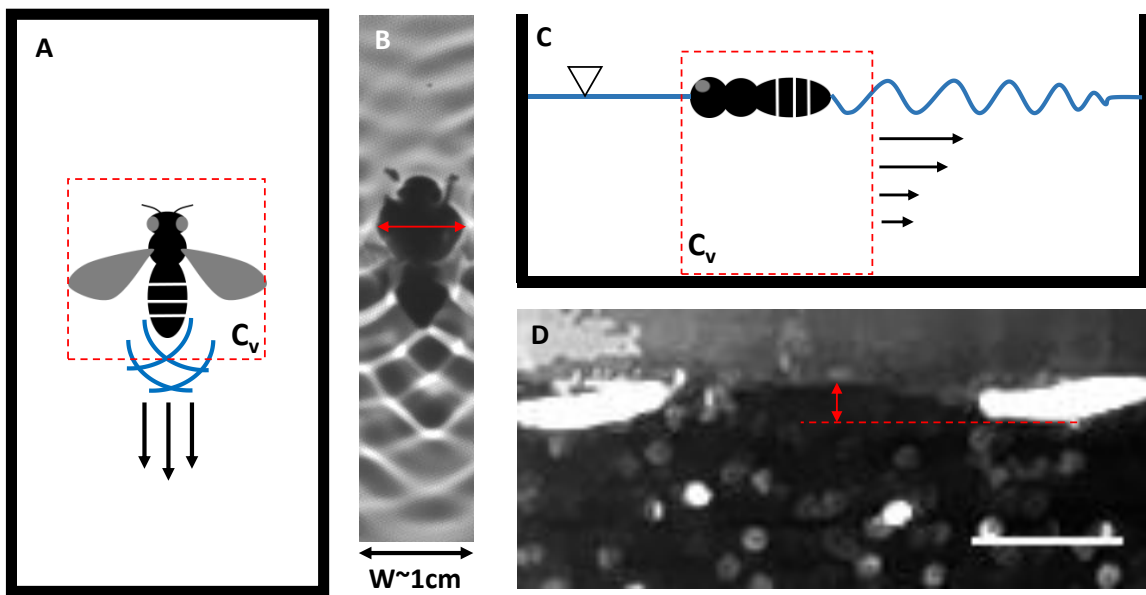


Figure 6.6 Control volume and parameter measurements. (A) control volume from the top view. (B) Region with most significant wave field asymmetry. Red arrow indicates the dimple made by the hairy thorax ($\sim 0.82 \text{ cm}$). The width of the strip is approximately 1 cm. (C) Control volume from the side view. (D) Wave amplitude measurement. Scale bar = 2mm.

6.3.4 Average force calculation from flow and wav field

Assumptions for calculating momentum carried by surface wave are as follows: (1) momentum carried by surface wave cancel each other except at the rear due to the mostly symmetric pattern (Figure 6.3A, 6.6B), (2) momentum is carried by the surface wave corresponding to the wing vibration frequency. In this particular case, frequency of 58Hz,

which by dispersion relation, corresponds to a surface wave with wavelength, $\lambda = 5.3$ mm.

Substituting the following values, $\sigma=0.072$ N/m, $a=2.5 \times 10^{-4}$ m, $k=2*\pi/\lambda=1186$ 1/m, $W=0.01$ m, to equation (6.5) gives $\overline{F_{wave}} \sim 47$ μ N.

Assumptions for calculating momentum carried by flow are as follows: (1) only the backward moving central jet contributes to the momentum, and (2) u is approximated with half of the maximum horizontal velocity. Substituting the following values, $\rho=10^3$ kg/m³, $u=1.5$ cm/s, $A=1 \times 10^{-4}$ m², to equation (6.3b) gives $\overline{F_{flow}} \sim 23$ μ N.

6.4 Discussion

The magnitudes of $\overline{F_{wing}}$, $\overline{F_{wave}}$, and $\overline{F_{flow}}$ are of the same order. Thus, both wave and flow appear to have substantial contribution to the propulsion of the honeybee. However, results in this chapter are calculated with some strong assumptions, and therefore should be received as estimates.

The force estimates can be improved in many ways. The average force generated by the wing can be confirmed with the direct force measurement. In addition to the average force, a transient force measure is necessary to fully understand the propulsion of the honeybee. The estimation of momentum carried by wave can be made more precise by amplitude measurement of the whole wave field. The estimation of momentum carried by flow can be made more precise by measuring the entire three dimensional flow field.

In this study, the interaction between the fluid flow and the surface wave is neglected. The fluid flow near the free surface can generate new wave or influence the existing wave. Likewise, a traveling surface wave induces flow underneath. The force estimations in this chapter did not attempt to distinguish the momentum carried by wave and flow. Therefore,

some overlap in the measurement is expected. A clear distinction between them is possible only in rare occasions. One example is the study of water-strider propulsion, where the impulse of the flow is marked by the presence of vortex dipole pairs (Hu and Bush, 2003).

PART 2 Concluding Remarks

In Part 2 of this thesis, the honeybee's propulsion at the air-water interface was studied. In chapter 5, progress was made in discovering a new surfing-like propulsion mechanism, in which a thin wing membrane is used to simultaneously push and pull on the water surface to generate thrust.

The newly found multimodal ability of the honeybee could be applied in improving insect-mimicking aerial drones (de Croon et al., 2015; Ma, Chirarattananon, Fuller, and Wood, 2013). With the growing interest in engineering drones that can move in both air and water (Floreano and Wood, 2015), the honeybee's propulsion mechanism could provide valuable insight for developers. However, the advantage of using the honeybee's surfing-like mechanism would not be in its efficiency, but more so in that no significant changes are required to the robot morphology. The efficiency of this mechanism can be improved if the generation of the forward moving waves is suppressed.

Another progress was made in calculating the average force generated by the honeybee. Albeit a rough estimate, the comparison of the average force calculated from body motion, wake, and surface wave analysis showed that both the deeper water jet and the surface wave carry significant momentum.

PART 2 References

Altshuler, D. L., Dickson, W. B., Vance, J. T., Roberts, S. P. and Dickinson, M. H.

(2005). Short-amplitude high-frequency wing strokes determine the aerodynamics of honeybee flight. *Proceedings of the National Academy of Sciences of the United States of America* **102**, 18213-18218.

Burghelea, T. and Steinberg, V. (2002). Wave drag due to generation of capillary-gravity surface waves. *Physical Review E* **66**, 051204.

Burrows, M. and Sutton, G. P. (2012). Pygmy mole crickets jump from water. *Current Biology* **22**, R990-R991.

de Croon, G., Percin, M., Remes, B. D. W., Ruijsink, R. and De Wagter, C. (2015). The DelFly: design, aerodynamics, and artificial intelligence of a flapping wing robot: Springer.

Floreano, D. and Wood, R. J. (2015). Science, technology and the future of small autonomous drones. *Nature* **521**, 460-466.

Hu, D. L. and Bush, J. W. (2010). The hydrodynamics of water-walking arthropods. *Journal of Fluid Mechanics* **644**, 5-33.

Hu, D. L., Chan, B. and Bush, J. W. (2003). The hydrodynamics of water strider locomotion. *Nature* **424**, 663-666.

Lee, D.-G. and Kim, H.-Y. (2009). The role of superhydrophobicity in the adhesion of a floating cylinder. *Journal of Fluid Mechanics* **624**, 23-32.

Lindauer, M. (1971). Communication among social bees.

Longuet-Higgins, M. S. and Stewart, R. (1964). Radiation stresses in water waves; a

physical discussion, with applications. *Deep Sea Research and Oceanographic Abstracts*, vol. 11, pp. 529-562: Elsevier.

Ma, K. Y., Chirarattananon, P., Fuller, S. B. and Wood, R. J. (2013). Controlled flight of a biologically inspired, insect-scale robot. *Science* **340**, 603-607.

Marden, J. H. and Thomas, M. A. (2003). Rowing locomotion by a stonefly that possesses the ancestral pterygote condition of co-occurring wings and abdominal gills. *Biological Journal of the Linnean Society* **79**, 341-349.

Moffett, J. O. and Morton, H. L. (1973). Surfactants in Water Drown Honey Bees 123. *Environmental Entomology* **2**, 227-231.

Morton, H. L., Moffett, J. O. and Martin, R. D. (1974). Influence of water treated artificially with herbicides on honey bee colonies. *Environmental Entomology* **3**, 808-812.

Mukundarajan, H., Bardon, T. C., Kim, D. H. and Prakash, M. (2016). Surface tension dominates insect flight on fluid interfaces. *Journal of Experimental Biology* **219**, 752-766.

Snodgrass, R. E. (1984). *Anatomy of the honey bee*: Cornell University Press.

Yang, E., Son, J. H., Sang-im Lee, P. G. J. and Kim, H.-Y. (2016). Water striders adjust leg movement speed to optimize takeoff velocity for their morphology. *Nature Communications* **7**.

Appendix 1: Jet deflection by asymmetrically placed orifice nozzle.

A simple pipe flow with orifice nozzles of varying degrees of asymmetry is tested (Figure A1). The pipe diameter, D_p , was 1 inch and orifice diameter, D_o , was 0.5 inch. Total of 6 orifice nozzles were machined with orifice center progressively shifted by 0.05 inch. The degree of asymmetry (DOA) of the nozzles, as defined in section 4.2.1, were 0, 0.1, 0.2, 0.3, 0.4 and 0.5, where DOA = 0 representing the centered orifice. The experiment was conducted at 5 different Reynolds number ($Re=D_o*U_{max}/\nu$) ranging from 380 to 1100. Figure A1 shows the resulting flow visualization. In figure A2, DOA is plotted with the mean angles of the velocity vectors. In finding the mean angle, the velocity vectors with magnitude larger than 95% of maximum velocity are considered. The result shows that the asymmetry in the nozzle can deflect the jet up to $\sim 10^\circ$, but angle of deflection has small dependence on Re within the tested range.

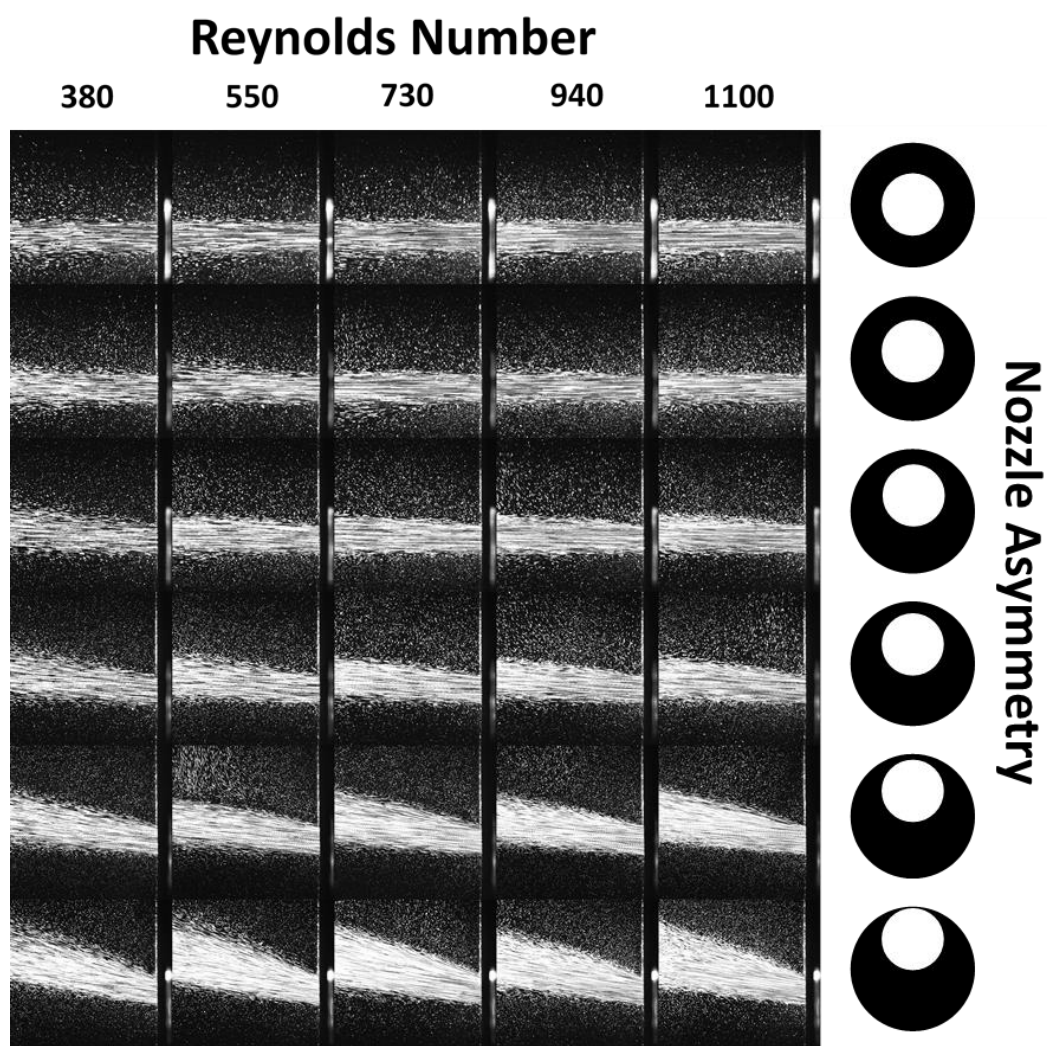


Figure A1. Jet emanating from the progressively asymmetric orifice nozzle.

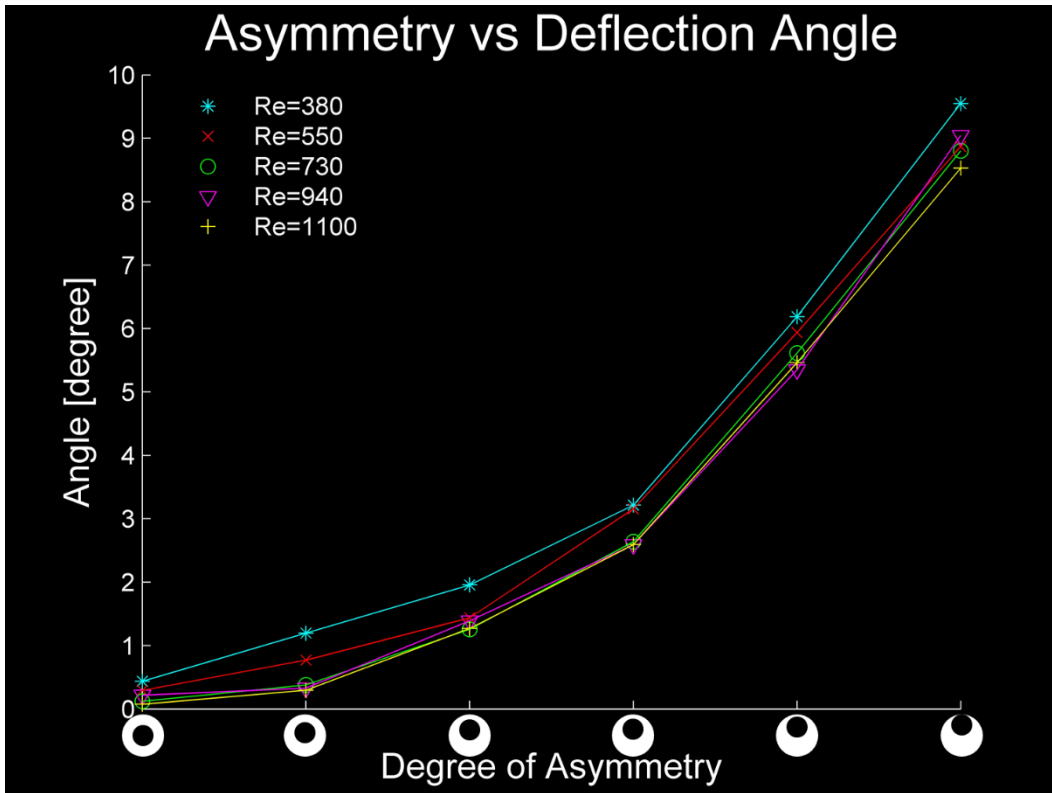


Figure A2. Degree of asymmetry vs deflection angle.